Masters Theses & Specialist Projects   Graduate School

Spring 2020

Quantifying Tekeze River Canyon Incision on the Ethiopian Plateau from Low-Temperature Apatite Thermochronology

Jacob Thomas Grigsby
Western Kentucky University, jacob.grigsby113@topper.wku.edu

QUANTIFYING TEKEZE RIVER CANYON INCISION ON THE ETHIOPIAN
PLATEAU FROM LOW-TEMPERATURE APATITE THERMOCHRONOLOGY

A Thesis
Presented to
The Faculty of the Department of Geography and Geology
Western Kentucky University
Bowling Green, Kentucky

In Partial Fulfillment
Of the Requirements for the Degree
Master of Science

By
Jacob Grigsby

May 2020

QUANTIFYING TEKEZE RIVER CANYON INCISION ON THE ETHIOPIAN
PLATEAU FROM LOW-TEMPERATURE APATITE THERMOCHRONOLOGY

Date Recommended _____May 13, 2020_____

Nahid Gani
Digitally signed by Nahid Gani
DN: cn=Nahid Gani, o=Western Kentucky
University, ou=Geography and Geology,
email=nahid.gani@wku.edu, c=US
Date: 2020.05.13 14:53:01 -05'00'

Nahid Gani, Director of Thesis

Stuart Foster

M. Royhan Gani

Jason Polk

_____
Cheryl D Davis Digitally signed by Cheryl D Davis
Date: 2020.06.01 11:58:56 -05'00'

Dean, Graduate Studies and Research   Date

ACKNOWLEDGEMENTS

TABLE OF CONTENTS

LIST OF FIGURES

LIST OF TABLES

LIST OF EQUATION
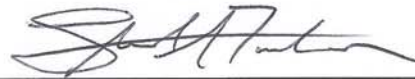
QUANTIFYING TEKEZE RIVER CANYON INCISION ON THE ETHIOPIAN
PLATEAU FROM LOW-TEMPERATURE APATITE THERMOCHRONOLOGY

Jacob Grigsby   May 2020   Pages 64

Directed by: Nahid Gani, Stuart Foster, M. Royhan Gani, and Jason Polk

Department of Geography and Geology   Western Kentucky University

The Ethiopian Plateau in East Africa features dynamic topography, deep river incision (~1.5 km), active tectonics, continental rifting, volcanic terrain and ~2 km of plateau uplift. Situated on the northwestern part of the Ethiopian Plateau, the Tekeze River is one of the two major rivers associated with incising and documenting the recent geologic history of the uplifted plateau landscape. The consequential Tekeze River incision into the uplifted Ethiopian Plateau is associated with the arrival and impingement of the Afar mantle plume as evidenced by the presence of thick sheets of Cenozoic flood basalts (~30 Ma). However, the Cenozoic to present-day incision history on the Ethiopian Plateau is poorly constrained relative to the number of published studies in the past few decades. In this study, the Cenozoic to present-day incision of the plateau is quantified from the Tekeze River by integrating low-temperature apatite (U-Th)/He and fission-track thermochronologic dating of crystalline basement rocks exhumed from the deep incisions carved out by the Tekeze River. Four samples were collected along a vertical section of the Tekeze River Canyon. Apatite (U-Th)/He and fission-track thermochronologic dating techniques were chosen specifically for their low closure temperatures and helium partial retention zone (PRZ), which better constrain the low-temperature cooling history of rocks to understand the Ethiopian Plateau incision. Inverse thermal history models were generated from HeFTy and QTQt modeling software.

New thermochronologic data from this study provides the youngest cooling ages to date in the study area. Results from the thermal history models indicate that the Cenozoic incision within the Tekeze River initiated ~28 Ma after the 30 Ma flood basalt event. Following this onset, incision continued until an ensued transition to exasperated incision rates occurred ~12 Ma, when the bulk of incision occurred, which is likely attributed to the base level perturbations. Incision timing remain unclear after the ~12 Ma due to model directional uncertainties.

1. INTRODUCTION

The Ethiopian Plateau (Fig. 1.1) spans a wide array of geologic features cataloguing a complex history of active tectonics evidenced from high topography and rivers that incise through its landscape (e.g., Pik et al., 2003; Gani et al., 2007; Abbate et al., 2015: Gani, 2015; Gani and Neupane, 2018; Xue et al., 2018). The Ethiopian Plateau, in other cases referred to as the Ethiopian Highlands, prominently displays ~1.5 km deep incised river canyons carved by the Blue Nile and Tekeze River networks (Fig. 1.2.) that provide a unique opportunity to study dynamic topographic processes, which ultimately led to the surface exposures of the deep residing bedrocks.

Several studies spearheaded the technique of low-temperature thermochronology to date and examine the timing and rates of incision at different plateaus in varying tectonic settings (e.g., Tibetan Plateau, Andean Plateau, Colorado Plateau) to constrain regional uplift (Gleadow and Brown, 2000; Clark et al., 2005; Schildgen et al., 2007; Flowers et al., 2008; and Nie et al., 2018). Numerous studies were done on the Ethiopian Plateau to better understand and quantify deep incision using various geochronologic techniques and geomorphic proxies (e.g., Pik et al., 2003; Gani et al., 2007; Gani, 2015; Blackburn, 2016; Gani and Neupane, 2018; Xue et al., 2018; Bowden, 2018). Among these, only a handful of low-temperature thermochronologic studies (Pik et al., 2003; Blackburn, 2016; Bowden, 2018) were conducted to constrain the plateau incision timing to understand its exhumation history. However, the timing of this incision is not universally agreed upon. Although these authors concluded the onset of the Ethiopian Plateau incision after the continental flood basalt volcanic event around ~30 Ma (Hofmann et al., 1997), the timing of post-30 Ma

plateau incision remains a challenge. With the emergence of additional geomorphic proxy

studies (Gani et al., 2007; Gani, 2015; Xue et al., 2018), the timing constraints found from
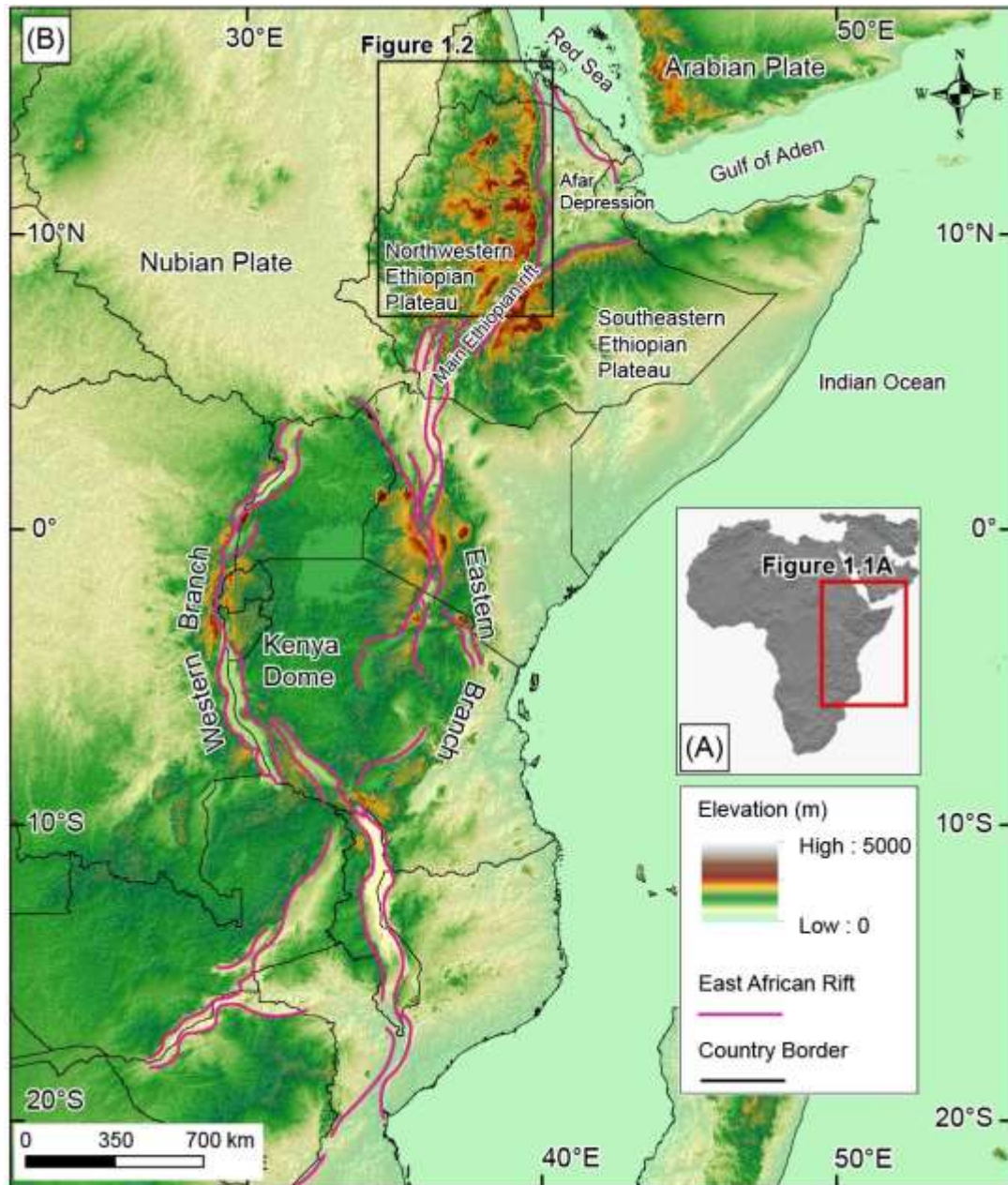
Figure 1.1: (A) Map of Africa showing East Africa. (B) Regional map of East Africa generated from Shuttle Radar Topography Mission (SRTM) Digital Elevation Model (DEM) illustrating the regional topography. The East African Rift system extents are highlighted with its Eastern Branch, Western Brach, Main Ethiopian Rift and Afar Depression. Notice the locations of the Northwestern and Southeastern Ethiopian Plateau and the Kenya Dome. The rectangle in (B) shows the location of Figure 1.2.
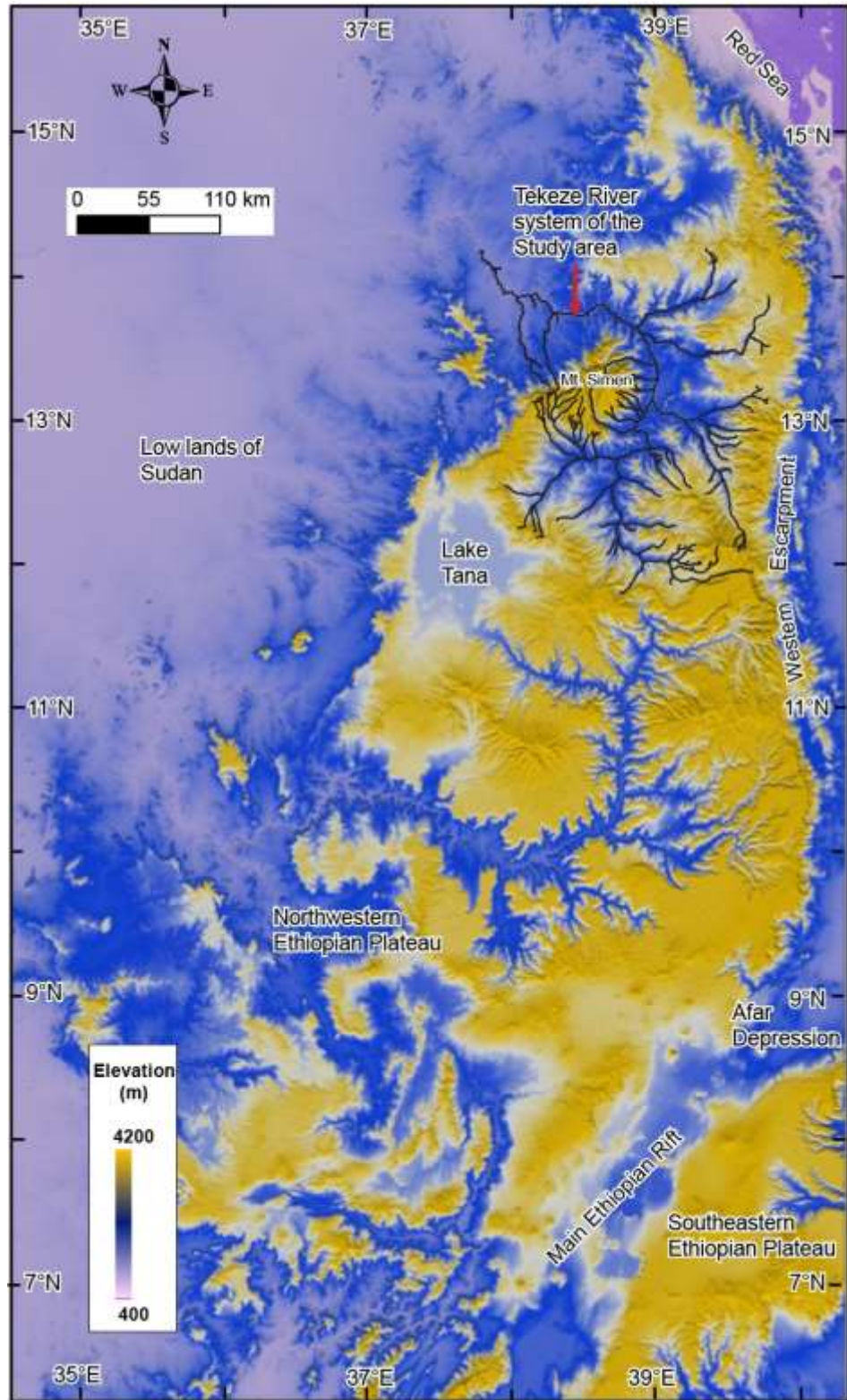
Figure 1.2: Shaded relief map. The shaded relief map of the Northwestern Ethiopian Plateau generated from SRTM DEM illustrating the Tekeze River of the study area in the norther part.

thermochronologic studies becomes more complicated. Existing evidences from geomorphic proxies (Gani et al., 2007; Gani and Neupane, 2018) show that the timing of river incision is episodic (Gani et al., 2007; Gani, 2015) and is controlled largely by topography related to mantle dynamics (Gani and Neupane, 2018). This discrepancy of incision timing of the Ethiopian Plateau has led to the speculations of differing geologic factors controlling this incision such as mantle plume-related domal uplift, variation in flood basalt thickness, and river discharge variability (Gani et al., 2007; Gani, 2015; Gani and Neupane, 2018; Xue et al., 2018). Thus, understanding the plateau incision using thermal history from the low-temperature thermochronology such as apatite (U-Th)/He and fission-track remains enigmatic and challenging. This challenges not only persist due to the timing variation but also due to the fact that the Cenozoic rocks resides close to the surface at the time of their exhumation since 30 Ma. Complications also arise due to the presence of thick sequence of Mesozoic rift-sediments and flood basalt on top of the basement rocks.

The majority of the low-temperature thermochronology applied to understand the timing and causes of incision was performed on the Blue Nile River network. In contrast, this study uses thermochronology in the Tekeze River network of the Ethiopian Plateau. The main objective of this research is to investigate the Tekeze River incision by low-temperature apatite (U-Th)/He and fission-track thermochronology of basement rocks (that is overlain by Mesozoic sedimentary rocks followed by the Cenozoic flood basalt and Quaternary volcanic rocks) in order to quantify the timing and causes of plateau incision. Results from this study provide new thermochronologic dates and thermal history to help refine the current complexities of the timing of the Ethiopian Plateau incision. In turn, this

can shed light on understanding the timing of plateau uplift related to mantle dynamics, and the interplay between tectonics, climate, incision and evolution of river-dominated landscape of the Ethiopian Plateau.
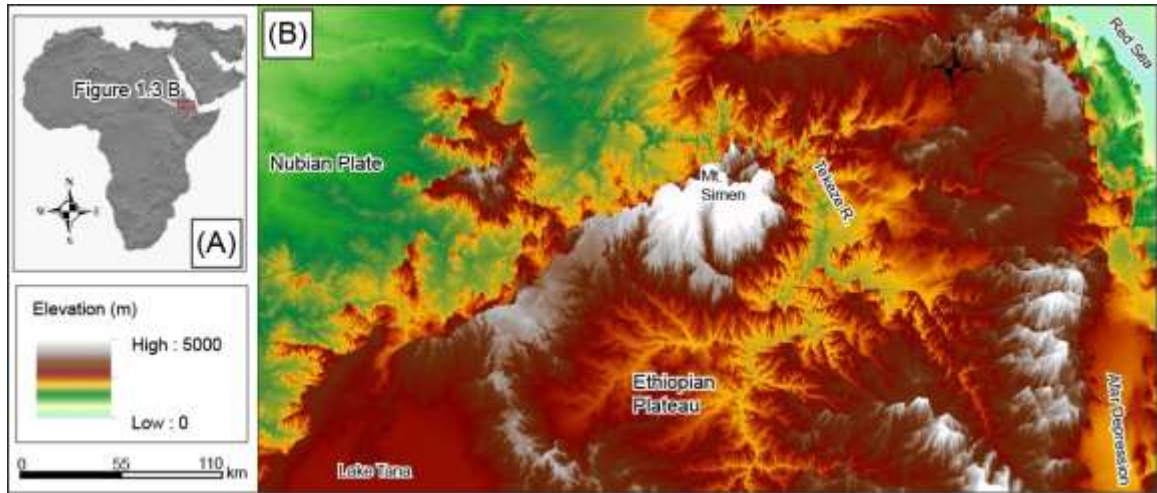
Figure 1.3: 3D view map of the Tekeze drainage. (A) Map of Africa showing location of Figure 1.3 B. (B) 3D perspective view of the northern part of the Northwestern Ethiopian Plateau generated from SRTM DEM showing Present-day topography and the Tekeze River.

2. GEOLOGIC SETTING AND TECTONIC HISTORY

The Tekeze River, situated within the Northwestern Ethiopian Plateau, is one of the major tributaries (Fig. 2.1) of the Nile River in Africa. The study area lies within the northern segment of the Plateau where the deepest incisions of the Tekeze River Canyon carved by the Tekeze River are most prevalent. The Tekeze River originates from Mt. Abune Yoseph at ~4,284 m elevation and flows northwest to drain into the Nile towards the lowlands of Sudan. The Tekeze River network is bounded by the Axum-Adigrat lineament to the north,
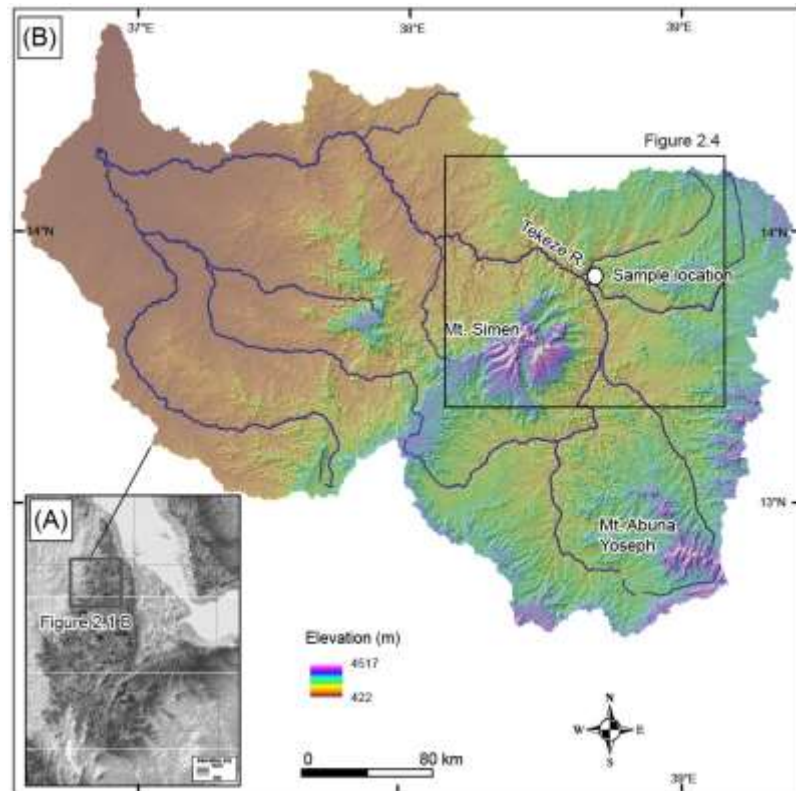
Figure 2.1: Tekeze drainage network. (A) Hillshade map of the Ethiopian Plateau showing the Tekeze River network. (B) Tekeze River network showing the extent of the Tekeze River and its tributaries among the delineated basin. The sample location is shown in the white circle, from which crystalline basement rock samples were collected for thermochronologic analysis. Notice the rectangle, which shows the location of Figure 2.4. (Image courtesy: Dr. Nahid Gani)

high escarpment related to the Afar Depression and the Red Sea Rift to the east, Mt. Guna

and Mt. Abune Yoseph to the south and Mt. Simen Ranges to the west. Widespread erosion

has persisted within this river network exposing a variety of lithologic units constituting

various periods of Ethiopia's geologic history that are summarized below.

2.1 East African Orogen, Basement Rocks and Structures

The initial tectonic event, the East African Orogeny (known as the East African Orogen,

EAO), spanned between 850-550 Ma (Fig. 2.2; Stern, 1994; Abdelsalam and Stern, 1996).

This event was most notably characterized by the development of banded iron formations,

eukaryote evolution, the breakup of Rodina, and most importantly, the protracted orogenic
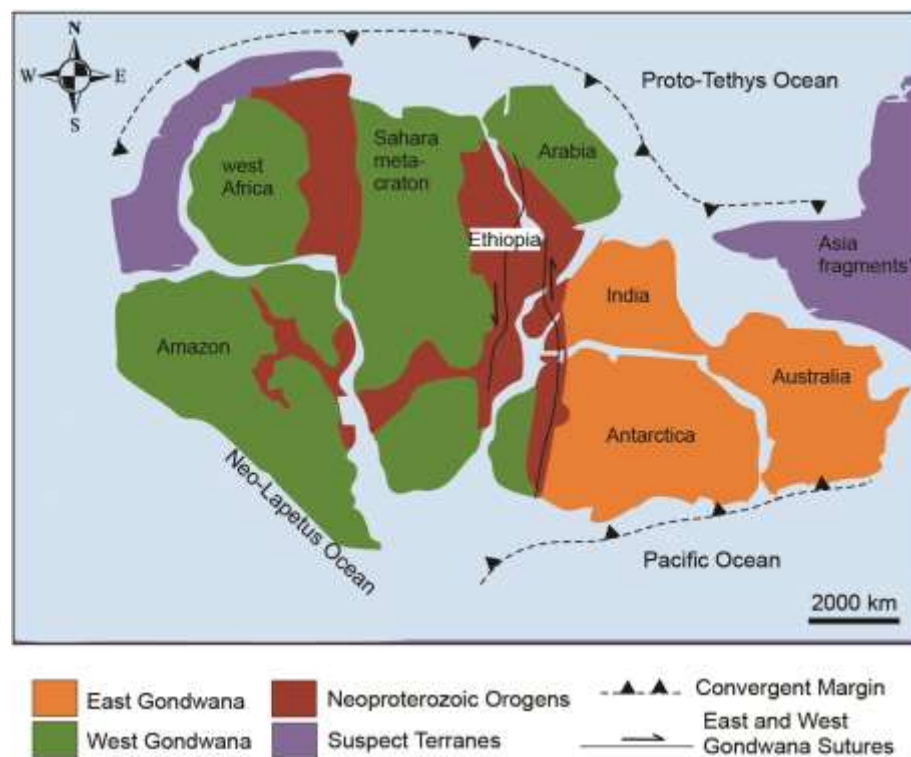
Figure 2.2: East African Orogen map (EAO) extent showing the collisional fabric associated with the formation of Gondwana during the Neoproterozoic. Mush of the pre-existing lineation from this Neoproterozoic event are responsible for the orientation of later rifting events.

cycle referred to as the "Pan African" orogenic cycle (Stern, 1994). The East African Orogeny was a result of the collision between East and West Gondwana that generated the north trending structure of the Arabian Nubian Shield (ANS) and the Mozambique Belt (MB). Both structures constitute the foliated and folded Neoproterozoic basement rocks overlain by younger sedimentary and volcanic rocks along the closure of the Mozambique Ocean (Stern, 1994). The Arabian Nubian Shield in the northern part of Ethiopia dominantly consists of metamorphic and plutonic rocks overlain by stromatolitic and diamictite sedimentary rocks from Snowball Earth (Beyth et al., 2003). Evidence for this collisional event also include the existence of observable N-trending compressional structural fabric from thrust faults and folds, which in later stages, developed shear components observable in the crystalline basement through superimposed dextral and sinistral movement within faults and folds (Fritz et al., 2013).

2.2 Paleozoic Glaciation, Mesozoic Rifting, Sedimentation and Structures

In the Paleozoic, after the formation of Gondwana, glaciations affected East Africa as the Southern Pangea Ice Sheet advanced and retreated, as evidenced from planation surfaces in outcrops (Bussert and Schrank, 2007). Glaciation removed much of the collisional fabric topography from the basement rocks in East Africa, leaving behind N-S trending glacial valleys. Glacial deposits primarily composed of conglomerates and siltstones deposited as a result of retreating ice sheets. In Ethiopia, the Endaga Arbi Tillites and the base of the Enticho Sandstone represent these Carboniferous to early Permian glacio-fluvial deposits (Bussert and Schrank, 2007). The erosion left behind few remnants of marine sandstones from the Ordovician and Silurian, with some conglomerated and

brecciated glacial deposits attributed to a massive glacial period at the end of the Paleozoic during the Pangea breakup (Abbate et al., 2015).

Gondwana began its separation forming a series of triple junction rifts throughout East Africa in the Early Mesozoic. Rift formation was largely guided by preexisting weak zones resulting from N-S trending structural fabric from the East African Orogeny. Evidenced by remnants of extensional stresses and meso-scale normal faulting, these preliminarily NW-SE trending rifts allowed for thermal subsidence and the formation of rift basin development throughout East Africa (Binks and Fairhead, 1992). The rift basin development from the Gondwana extension directly influenced the later geologic events. Most of the uplifted rift flank margins of the Mesozoic rifts provided the sources of siliciclastic materials to fill the rift basins, which became denudated throughout the largest marine transgression that lasted from the Triassic to the Kimmeridgian (Gani et al., 2009).

The formation of three related rift basins (Fig. 2.3) was recognized throughout this time period in Ethiopia incorporating the Blue Nile to the west, the Ogaden Basin to the east, and the Mekele Basin to the northwest (Abbate et al., 2015). The three basins had similar sedimentation histories, and likely were members of an initial Mesozoic triple junction, even though the Ogaden Basin comprises of a large sediment accumulation with a different depositional history through Late Mesozoic-Early Cenozoic (Hunegnaw et al., 1998). Early rifting during the Mesozoic is signaled with the unconformable deposition of the Adigrat Sandstone in the Early-Late Jurassic, containing fluvio-lacustrine rift-related sediments. The Glauconitic Sandy Mudstone unit forming the top of the Adigrat Sandstone indicated a marine transgression during the Middle Jurassic (Gani et al. 2009). The

mudstone unit is conformably overlain by the Antalo Limestone, which marks further marine transgression within the Blue Nile Basin and Mekele Basin (Fig. 2.4.).
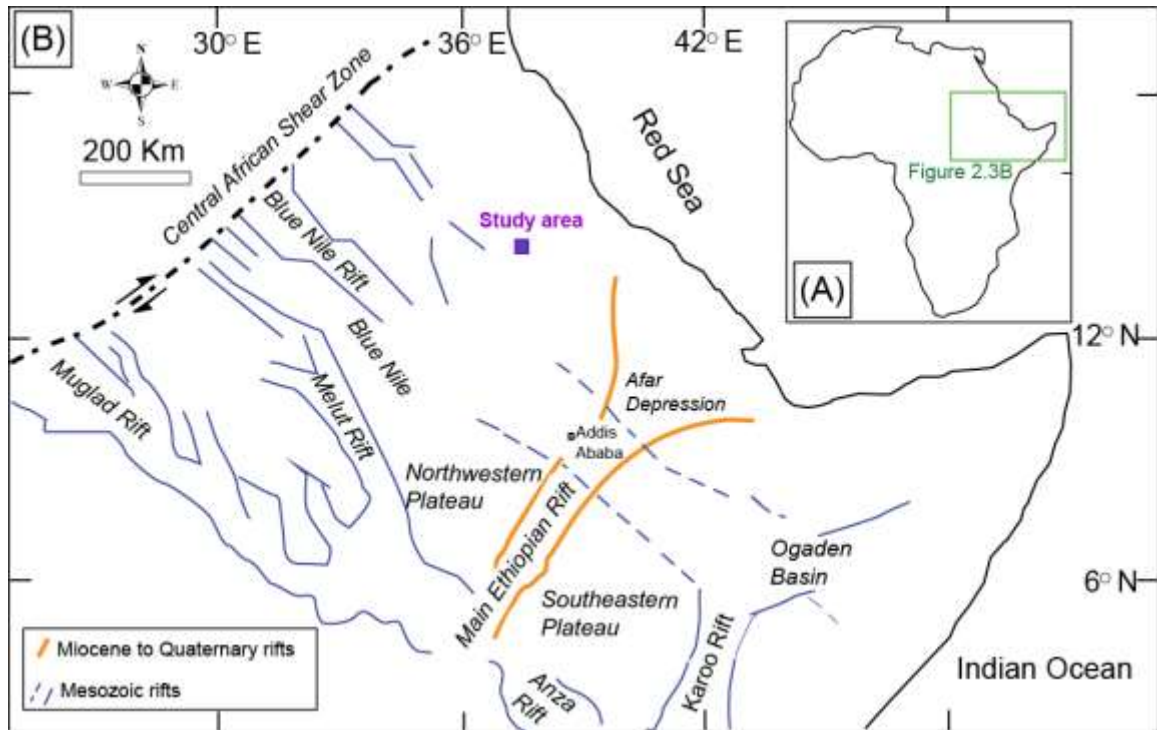
Figure 2.3: Mesozoic rift map. (A) Map of Africa shows the location of figure 2.3 B. (B) Mesozoic rifts within the Ethiopian Plateau. Mesozoic rift structures (blue) are shown to have a predominant NW-trend, compared to the NE-trend of the Miocene to Present-Day Main Ethiopian Rift and Afar Depression (orange). Notice the location of the study area (modified from Gani et al., 2009).

A marine regression was evidenced in the Blue Nile and Mekele basins with the deposition of the fluvial Amba Aradam Sandstone in the Early Cretaceous, which is followed by a long hiatus (Abbate et al., 2015). This regression occurred concurrently with the hiatus and followed with the transition of the Somali-India rift taking over to the east (Corti, 2009). The Ogaden Basin varied from the other two Ethiopian Basins in the Cretaceous, with repeated marine transgressions and regressions. These cycles indicate that

the Ogaden Basin rift had also failed causing the basin to enter a passive margin cycle in

the Cretaceous that lasted through the early Cenozoic.
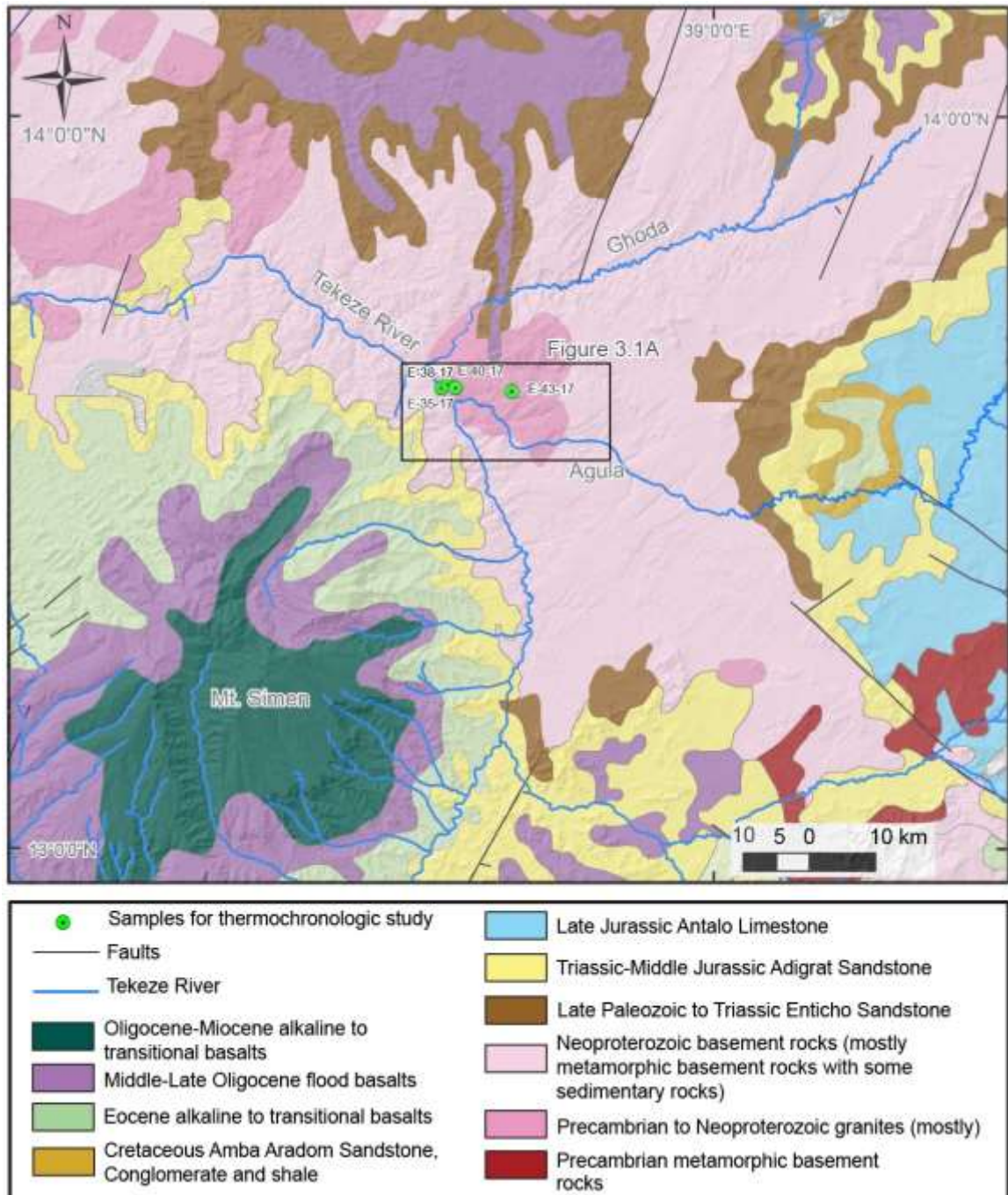
Figure 2.4: Simplified geologic map of the study area including major rock units, faults, and sample locations. (modified after Mangesha et al., 1996; Gani, 2015). The extent of this map is shown in figure 2.1 B.

2.3 Cenozoic Mantle Plume Impingement and Continental Flood- Basalt Volcanism

Amidst the Cenozoic during the Oligocene, the African Superswell plume(s) became emplaced below Ethiopia, signaled by widespread flood-basalt volcanism (Marty and Gezahegn, 1996; Hofmann et al., 1997).

Numerous studies have been conducted in large efforts to observe and characterize the dynamics of the large mantle plume resting beneath Africa (Ebinger and Sleep, 1998; Ring, 2014). From the aforementioned studies, the African Superswell plume was regarded as the driving mechanism of uplift and rifting as it shifted from Zambia to its current residence under Ethiopia and Kenya. Ebinger and Sleep (1998) characterized the Ethiopian and Kenyan volcanism sourced from a single plume with variations among the volcanic events attribute to regions of preexisting weaknesses in the lithosphere. George and Rogers (2002) suggested two separate and distinct mantle plumes reside below the Kenyan Dome and the Ethiopian Plateau, based on geochemical differences in associated volcanic episodes. The early eruptions occurred between 45-35 Ma classified as a basaltic plume signature, while the more recent Tertiary eruptions between 19-11 Ma had a more evolved continental lithospheric signature. Furthermore, the results suggested instead of one large plume, the African Superswell could likely be a result of heterogeneous secondary plumes deriving from a larger African Superplume within the core-mantle boundary (Civiero et al., 2015). The seismic S and P wave tomographic study of Davis and Slack (2002) suggested that distinct and separate domes residing beneath Ethiopia and Kenya, while Civiero et al. (2015) provided evidence supporting further complexities with multiple smaller scale shallow mantle plumes. Thus, the plume-related volcanism in Ethiopia erupted a thick succession of continental flood basalt, which uncomfortably lie on the

preexisting Mesozoic rift related sedimentary rocks. Mohr (1983) estimated that these flood basalts covered more than 750,000 km^2 of volcanic rocks. Based on magnetostratigraphy and ^{40}Ar/^{39}Ar analysis, Hofmann et al., (1997) concluded the eruption age for these flood basalts of ~30 Ma (Fig. 2.4). The thicknesses of these basalts at present within the Northwestern Ethiopian Plateau ranges between 500-2000 m across, with lesser thickness at the north (Gani, 2015).

2.4 Afar Depression and Cenozoic Ethiopian Rift Development

The western region of the Ethiopia Plateau's landscape is attribute to the complex interplay of structural events during the Cenozoic. The study area is distinguished by the interaction of the domal uplift concurrent with Cenozoic volcanism, flexural uplift of the rift-flanks, and extensional structures from the Main Ethiopian Rift, Afar Depression and the Red Sea rifting.

The Main Ethiopian Rift is representative of rifting process in the larger chain of the East African Rift, which stretches from southern Africa to the Afar Depression (Fig. 1.1). The Afar Depression contains three main branches extending from the Red Sea Rift trending northwest, the Aden Ridge in the Gulf of Aden trending northeast, and the East African Rift trending southeast.

The East African Rift system follows an archetypal rift pattern analogous to observed early stages of continental rift development on passive margins before continental separation and seafloor spreading (Chorowicz, 2005). Pre-existing Gondwana rift features played a significant role in the present rift structure, with rift basins stretched throughout East Africa following pre-existing weaknesses and pathways from old pre-rift suture zones

(Versfelt and Rosendahl, 1989; Corti, 2009). The East African Rift system splits off from the Afar Depression into two branches of subsiding graben, with the Main Ethiopian Rift constituting in the northern segment (Corti, 2009).

The Main Ethiopian Rift, making up the northern section and eastern branch of the East African Rift system, is defined by a symmetrical normal faulted bounded rift system (Woldegabriel et al., 1990; Chrorwicz, 2005). Efforts have been made to date the initiation of rifting, with ^{40}Ar/^{39}Ar dates from Ebinger et al. (1993), suggesting the extension did not begin until 18-14 Ma whereas, Wolfenden et al. (2004) used a similar methodology to conclude the Main Ethiopian Rift did not activate until 11-8.3 Ma. Bonini et al. (2005) proposed that the Main Ethiopian Rift began and lasted from 21-11 Ma, with localized southward-propagated deformation occurred during 10-5 Ma, followed by a reactivation of the Main Ethiopian Rift from 5-3 Ma. With the occurrence of rifting, uplift, and volcanism across the study area, sedimentation adjusted over the Cenozoic. With the rise of the landscape, concurrently came the development of intertrappean (flood basalt) beds ranging from tens to hundreds of meters in thickness.

2.5 River Incision and the Ethiopian Plateau Uplift

Affiliated with convective mantle plume emplacement and upwelling is the large bulge of uplift, which occurred throughout much of the Ethiopian landscape. The magnitude of the uplift across Ethiopia averaged ~2 km (Yemane et al., 1985; Abbate et al., 2015). Abbate et al. (2015) agrees that uplift of the Ethiopian Plateau initiated sometime after the widespread flood basalt event ~30 Ma, meaning that basalt was placed rather homogenously before present day topography and incision features existed. Multiple studies characterize the Ethiopian Plateau uplift and incision.

Paleoflora studies have been conducted on the Ethiopian Plateau to determine uplift. Vegetation fossils dated ~8 Ma indicated a previous climate comparable to that of a lowland rainforest in areas uplifted 2000 m at present. Across the last 8 Ma lacustrine paleoflora indicates nearly 2000 m of uplift (Yemane et al., 1985; Adamson and Williams, 1988).

Pik et al. (2003) concluded from thermochronologic study that the majority of incision initiated between 29 and 25 Ma and that the present-day elevated topography of the Ethiopian Plateau has existed since Late Oligocene. Gani et al. (2007) conducted a study quantifying river incision on the Northwestern Ethiopian Plateau through the geochronology-based geomorphic approach of investigating river longitudinal profiles, knickpoint data, and field analysis within the Blue Nile River system. This study concludes three phases of incision (ca. 29–10 Ma, ca. 10–6 Ma, and ca. 6 Ma to present) incision increased rapidly around from 10 Ma and 6 Ma,

Spiegel et al. (2007) applied apatite fission-track and (U-Th)/He dating to the Kenyan rift system. Results indicated younger ages of rifting in East Africa prevalent in the late Neogene. While not directly constraining uplift in Ethiopia, this supports active tectonics and uplift in the Neogene. Pik et al. (2008) studied the uplift history through the application of apatite (U-Th)/He thermochronology methods to date the border fault exhumation of the Main Ethiopian rift as a proxy for uplift. The results indicated pre-rift elevation of 600-800 m, and a later study by Gani (2015) used similar methods in the Tekeze River system to also conclude a three-phase incision, which dictate an incision rate increase ~10 Ma suggesting a total uplift of 2,200 m occurred with a majority of it taken place during the Oligocene.

3. MATERIALS AND METHODS

3.1 Introduction

In order for river incision to occur, a river must be supplying sufficient discharge and power across the landscape over a consistent and long period while rock erodibility and shear stress factors including the cohesion of bedrock, sediment supply, grain size and composition, plucking, abrasion, and weathering must be sufficient. Howard et al. (1994) explain river incision is one of the most important erosional processes responsible for changing the landscape in response to perturbations in surface uplift and climate. A stream in an uplifted region will preferentially carve into the bedrock until reaching base level, at which point erosion will slow or cease. This relationship indicates stream erosion is indicative of uplift (Humphrey and Konrad, 2000; Wakabayashi and Sawyer, 2001).

Quantifying past incision can be a daunting task, but proxies can approximate incision amounts and timing. Stream incision occurred millions of years ago is difficult to directly measure on the field, leading the necessary development of unique techniques to quantify incision rates and timing. One often-used tool for determining incision timing is low-temperature thermochronology. In areas where that area has undergone incision within the upper 1-3 km of the crust, several groups (Gleadow and Brown, 2000; Clark et al., 2005; Schildgen et al., 2007; Flowers et al., 2008; Rohrmann et al., 2012; Nie et al., 2018) have pioneered the use of low-temperature thermochronology to date incision as a function of exhuming buried rocks, and by extension, uplift timing.

In this study, basement rock samples were collected during a 2017 field season as part of the American Chemical Society Petroleum Research grant funded project. These

rocks were collected along a vertical profile across the Tekeze River Canyon in sequential elevations ranging from 800 m to 1500 m (Fig 3.1). Collecting thermochronology samples across a vertical section helps to further ensure that the timing from modeled cooling ages reflects incision history in this study. Further measures on the field were taken to ensure rock samples collected were not weathered or located in the proximity to any faults, igneous intrusions, and magmatic bodies, thus, ideally preserving the cooling age that is likely resulted from exhumation caused by river incision.
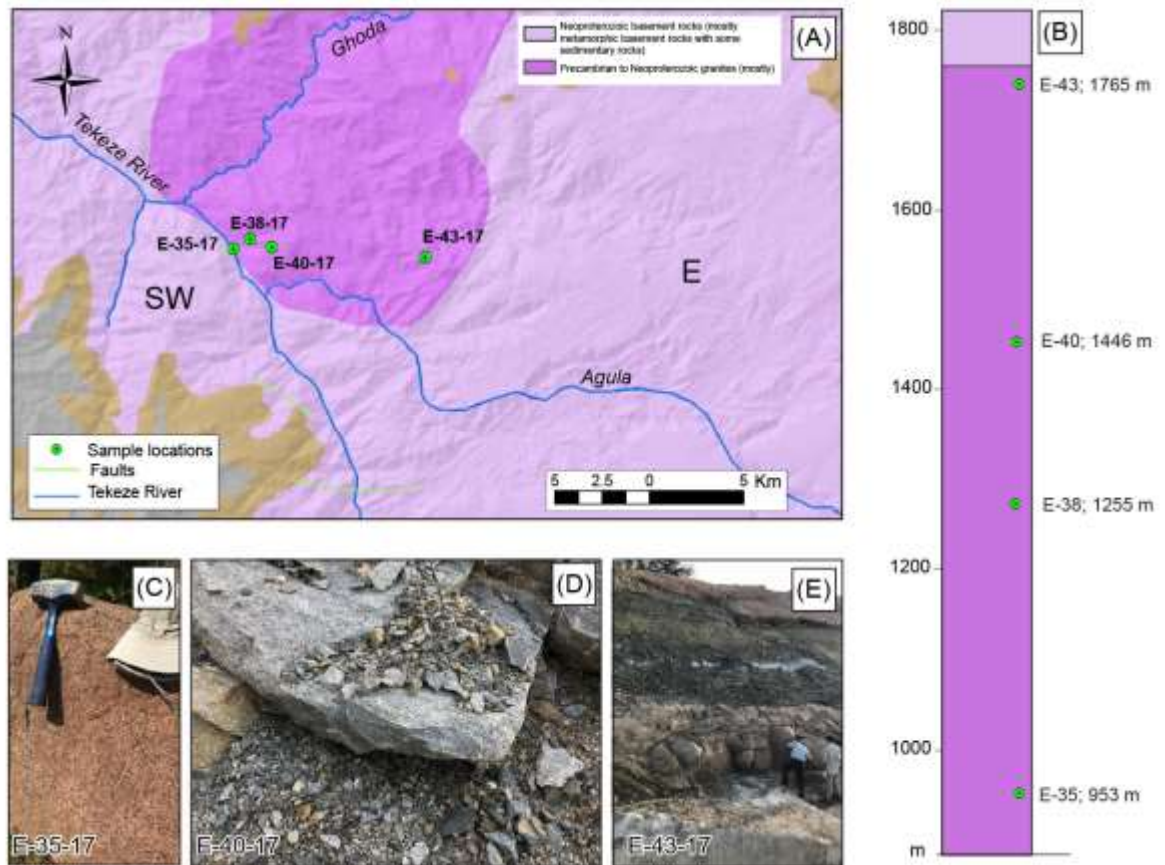
Figure 3.1: Vertical section and sample location. (A) Close-up view of the geologic map, the extent of which is shown in figure 2.4. (B) Stratigraphic column showing crystalline basement rock samples collected for thermochronologic study. (C) Sample E-35-17 shows Precambrian to Neoproterozoic granites. (D) Sample E-40-17 shows Precambrian to Neoproterozoic granites. (E) Sample E-43-17 shows Precambrian to Neoproterozoic granites.

3.2 Sampling Methods: Rock Sample Processing and Mineral Separation

Collected samples were initially processed at Western Kentucky University's Landscape Geodynamic (LeGo) lab before thermochronologic dating was conducted at Arizona State University's Group 18 Laboratory and GeoSep Services. The goal of sample processing was to reduce rock samples into separated apatite minerals in a way which is sustainable, cost effective, and limits potential contamination from occurring. A description of the sample processing is summarized in Fig 3.2.

Sample Processing Overview

1. Crush Rock — 2. Wash Mud and Sand Particles — 3. Sieve to <355 microns

4. Density separation of minerals using Lithium Metatungstate (2.95 g/cc) — 5. Magnetic separation of minerals at .5 amps

6. Magnetic separation of minerals at 1.0 amps — 7. Evaluation of minerals using Scanning Electron and Petrographic Microscopy
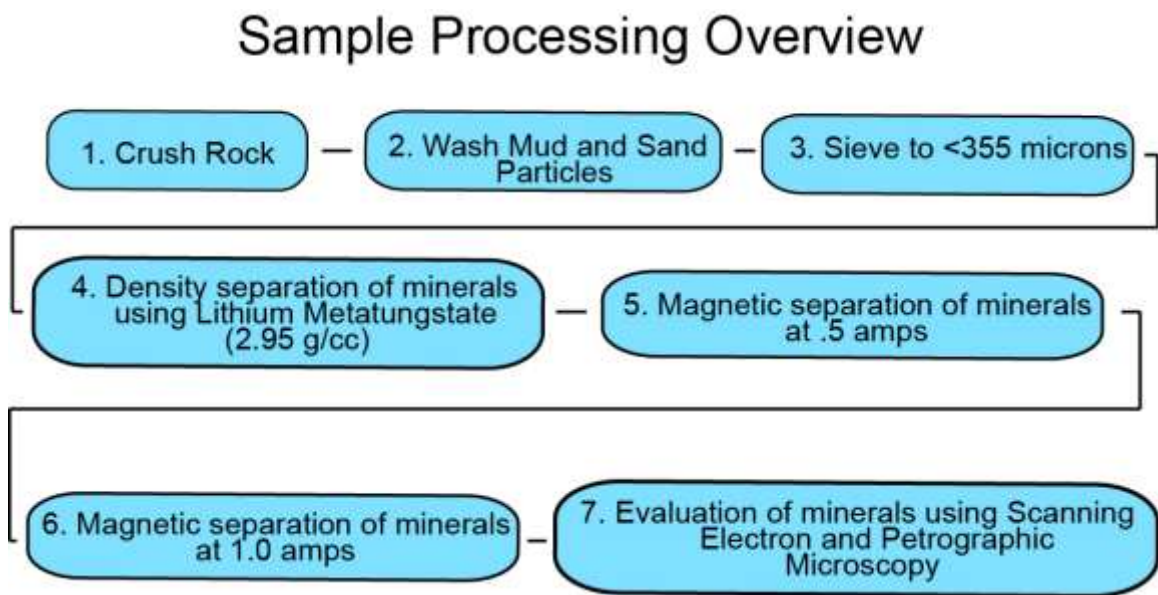
Figure 3.2: Sample processing overview. Basement rock sample processing steps performed at the LeGo (Landscape Geodynamics) lab for mineral separation and evaluation. At the LeGo lab, samples are separated into their mineral components, and evaluated before being sent off for thermochronologic dating analysis.

Samples were washed of loose dirt and particles before crushing them into small fragments using a Bico Chipmunk Jaw Crusher. After crushing, loose particles were once again washed using cold water and sieved into a 355-micron mesh. The micron mesh size was constrained to 355-microns as larger rock fragments are observed to contain minerals

cemented in matrix, thus further crushing and sieving the fragments would destroy the minerals.

The sieved grains <355-microns were then subjected to heavy liquid separation by using lithium metatungstate (LMT). LMT contains a specific gravity of ~2.93 g/ml, ideally denser than quartz and most feldspars. Separation with LMT was attained by mixing sieved grains with appropriate amounts of LMT into centrifuge tubes. Centrifugation was achieved running at 5000 and 7000 rpm for two minutes using an IEC Clinical Centrifuge. Minerals with a specific gravity > 2.93 (i.e., apatites and zircons) sink while minerals with a specific gravity <2.93 floated and were easily removed from the centrifuge tubes. Multiple iterations of LMT separation process are applied in attempt to prevent phyllosilicates from blocking dense minerals from dropping.

The mineral grains separated by LMT were subjected to a three-step magnetic separation process using hand magnets and an isodynamic magnetic separator. Strongly magnetic minerals, such magnetite, were removed by using a hand magnet. Following hand magnet separation, the isodynamic magnetic separator was used. With the isodynamic magnetic separator, an electric field was created, which in turn develops a magnetic field between two poles with a track allowing minerals move down and separate according to attraction and magnetic susceptibility. Two ramp runs, at 0.5 amps, followed by multiple iterations of 1.0 amps, were applied to remove minerals of different magnetic susceptibility than apatite.

The resultant separated suite of minerals bearing intrinsic properties of apatites were then evaluated and picked using binocular and petrographic microscopes. Beyond these microscopes, the quality of minerals was further assessed to limit error through

mineral imperfections using Scanning Electron Microscopy in conjunction with X-Ray Electron Dispersive Spectroscopy. Large euhedral minerals free of inclusions are selected to best limit error when undergoing thermochronologic dating. Sample processing finalizes with having at least 4 quality remaining apatites minerals being selected to represent each rock sample for thermochronologic dating.

3.3 Thin section analysis

In addition to mineral samples, thin sections were made from the samples to investigate "bad neighbor" effect. Nearby mineral grain (bad neighbor) within the rock can
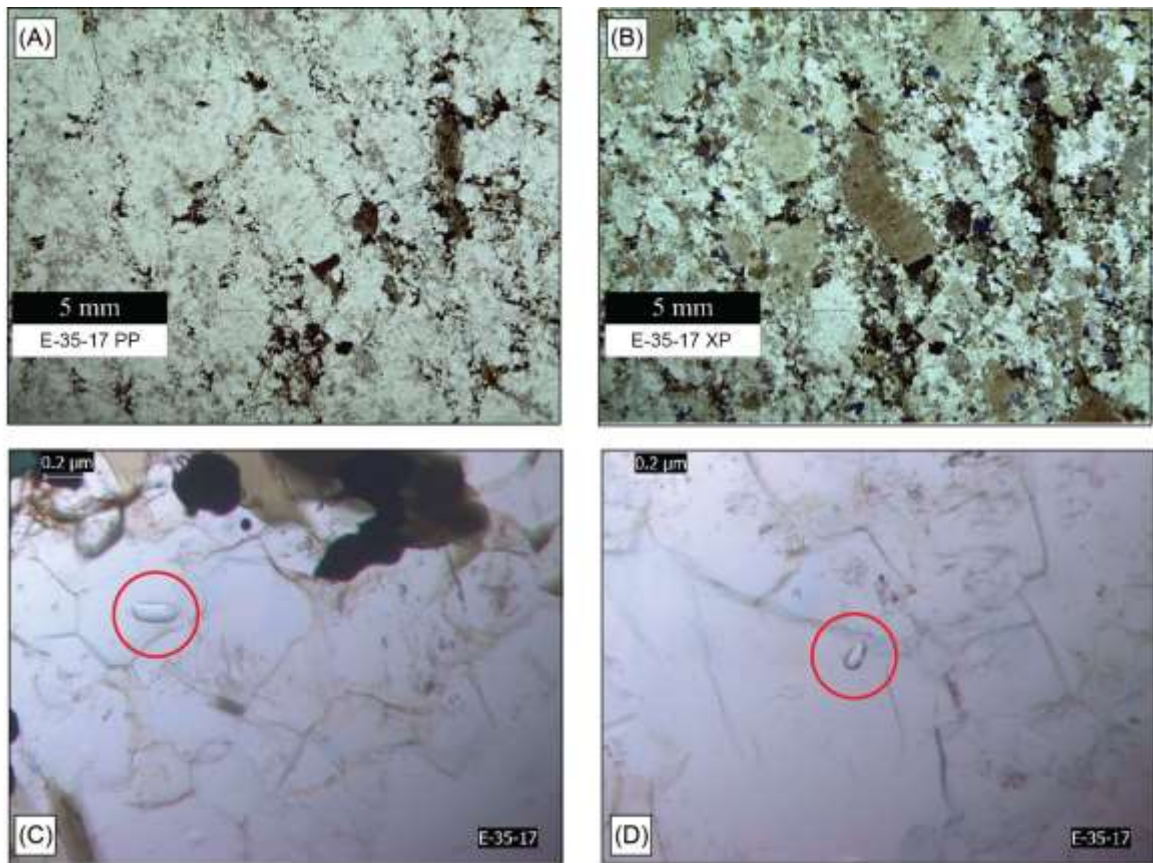
Figure 3.3: E-35-17 thin section. (A) Plain polarized light and (B) cross-polarized light images of sample E-35-17 (C) and (D) are magnified plain polarized images of sample E-35-17, which shows examples of apatite circled in red with no example of potential He implantation found.
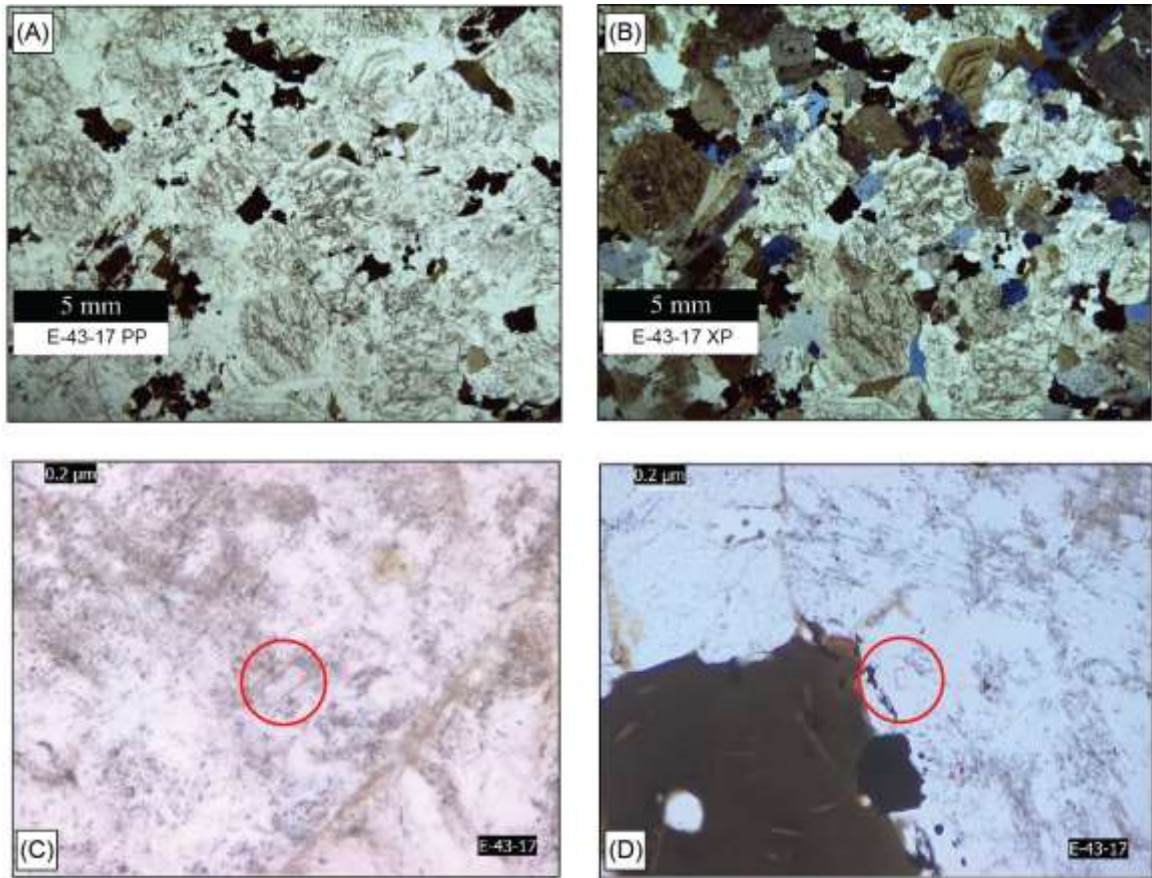
Figure 3.4: E-43-17 thin section. (A) Plain polarized light and (B) Cross-polarized light images of sample E-43-17. (C) and (D) are magnified plain polarized images of sample E-43-17, which shows examples of apatite circled in red with no example of potential He implantation found.

eject illegitimate daughter (4He) elements into other mineral grain within alpha-recoil stopping distance, potentially skewing cooling ages to older ages than what they actually are. Thin sections were prepared using standard procedures at the National Petrographic Laboratory (Figs. 3.3 and 3.4). Thin sections were prepared using the standard operating procedures from rock billets to 25x50 mm thin sections. Each of this section is analyzed under petrographic microscope using plane and cross-polarized lights. Analysis of these

thin sections assists in verifying inaccuracy of cooling ages with respect to the bad neighbor effect.

3.4 Low-Temperature Thermochronology Background

Thermochronology in its pure essence is the evaluation of the thermal history of rocks and minerals. From a geologic standpoint studying shallow crustal processes, thermochronology is best applied at cool temperatures below 300 $^{\circ}$C in the crust. In this premise, the type of thermochronology applied is confined to the subset of low-temperature thermochronology. With the use of low-temperature thermochronology, the cooling age as well as the complete thermal history of a mineral can be obtained, whereas in geochronologic studies, only the single absolute cooling age can be designated (Reiners et al., 2005). This advantage allows for both rates and ages of processes to be evaluated.

The practice of thermochronology for past 30 years has been reliant on the measurement of natural radioactive decay through measurement of unstable parent isotopes and accumulated daughter products to determine the cooling age of minerals. In thermochronologic studies, the cooling age represents the time at which a mineral has passed through a specific temperature, known as the closure temperature (Dodson, 1973). When a mineral is above the closure temperature, the decay product of the system, ^{4}He, will diffuse through and out of the grain and will not be retained. The concept of closure temperature varies depending on the type of thermochronometer used. Realistically, closure temperature behaves as a gradational window more than a boundary, during which the daughter isotopes will be retained. The range of temperatures at which closure temperature envelopes and minerals begin to retain daughter isotopes is called the partial retention zone. Ratios of parent-to-daughter isotopes determine the cooling at age which

minerals begin to retain daughter isotopes, and aids in reconstructing a minerals partial retention zone (Reiners et al., 2005). The partial retention zone is malleable, and subject to change from a variety of factors including pressure, mineral quality, and mineral size. Measured and studied from stepwise degassing experiments (Shuster and Farley 2003, 2005), the understanding of mineral diffusivity has improved to allow better interpretations, such as larger minerals having higher and wider partial retention zones, and higher pressures attributing to increased partial retention zone temperatures of minerals. With the assumption of a generally stable geothermal gradient, isotherms can be inferred within the subsurface, relating to the partial retention zone and age of a mineral in order to decipher complete depth and temperature histories of minerals (Reiners and Brandon, 2006).

Thermochronology techniques are applied to apatites in this study for its advantageous low closure temperature capabilities. Having lower closure temperatures is best for providing near surface thermal history at shallower depths with greater sensitivity. The chemical properties of apatite dictate that diffusion of daughter element ^{4}He occurs until temperatures drop blow ~80-100 °C undergoing (U-Th)/He dating and 100-120 °C fission-track dating (Reiners et al., 2005).

3.4.1 Apatite (U-Th)/He Dating

(U-Th)/He dating involves the measurement of the accumulated alpha particles (^{4}He) produced at a consistent rate during the radioactive decay chain process of ^{238}U, ^{235}U, ^{232}Th (and ^{147}Sm by a partly insignificant amount) to their daughter products (Ehlers and Farley, 2003). The radioactive production of ^{4}He can be expressed by the following equation:

$$^4He=8^{238}U[\exp(\lambda_{238}t)\text{-}1]+7^{235}U[\exp(\lambda_{235}t)1]+6^{232}Th[\exp(\lambda_{232}t)\text{-}1]+1^{147}Sm[\exp(\lambda_{147}t)\text{-}1]$$

Equation 1: U-Th/He Age Calculation. In this equation, the measured atoms are 4He. 238U, 235U, and 232Th, the λs are the decay constants, and t is the helium accumulation time also known as the (U-Th)/He age (Reiners, 2002; Ehlers and Farley, 2003).

(U-Th)/He dating is used to measure the time at which the mineral apatite cooled as the Tekeze River incised and exhumed rocks from Earth's crust. In the apatite (U-Th)/He thermochronology system, naturally occurring radioactive isotopes ^{238}U, ^{235}U, ^{232}Th, and ^{147}Sm undergo constant radioactive decay. If the apatite is hot (not near the Earth's surface), it releases radioactive daughter isotopes ^4He, which are able to diffuse out of the mineral.

(U-Th)/He data of 16 apatite minerals from four rock samples were conducted at the Arizona State University's Group 18 Laboratory. Selected apatite minerals were imaged and measured for fission-track age correction. After evaluation, samples were loaded into platinum tubes before being subjected to irradiation via infrared laser. He isotope concentrations were determined through ratio measurements with quadrupole He mass spectrometry. Platinum tubes containing degassed minerals were placed into acid solution, to be dissolved and then parent isotope concentration were measured ICP-MS (Inductively Coupled Plasma Mass Spectrometry). After data acquisition of U, Th, and He concentrations, the aforementioned formula was used to calculate (U-Th)/He ages. Relative standard error was calculated based on error throughout the replicate heating and degassing during the subsequent analytical He, U, and Th isotopic measuring process (Reiners and Brandon, 2006). Table 1 shows the apatite (U-Th)/He dating results for all the samples in this study.

3.4.2 Apatite Fission-Track Dating

In fission-track thermochronology, cooling ages are obtained by measuring the density of fission damage tracks left over by the parent ^{238}U isotopes. Fission reactions caused by the parent ^{238}U isotope's radioactive decay results in the splitting of decaying isotopes into two pieces that repel one another with great energy. As a result of the repulsion energy, damage paths are left behind in the minerals that range from 1-15 µm. Once the mineral cools below its closure temperature (100-120°C in fission-track dating) the damage trails are preserved allowing the density of fission tracks to be measured in the mineral for determining cooling ages. This resultant fission-track cooling ages are also used to model and determine the age of river incision along with the (U-Th)/He dating results.

Apatite fission-track dating was performed at the GeoSep Services facility in Moscow, Idaho. Apatite fission-track thermochronologic ages were determined through the use of LA-ICP-MS (laser ablation inductively coupled mass plasma mass spectroscopy) in conjunction with analysis of U-Pb grain ages. Lengths were measured based on parameters of Dpar, confined track lengths, and inclination angles. In analysis, apatite samples were polished and etched in 5.5 N HNO3 for 20.0s at 21°C and irradiated with 252 °Cf fission fragment to enhance measurements of confined track densities and improve data quality. Table 2 shows the apatite fission-track dating results for all the samples in this study.

3.5 Thermal History Modeling

Used alone, cooling ages obtained from the low-temperature thermochronology do not provide enough information to interpret cooling as a result of incision in this study. To

adequately interpret cooling age as a result of incision, multiple sample cooling ages are measured from analytical techniques and grouped into inverse t-T thermal history model solutions. Thermal history models were generated for all of the data on an individual and sample group basis. Each apatite mineral was analyzed with an emphasis on the youngest cooling ages providing the most information relevant to the post 30 Ma thermal history. QTQt and HeFTy thermal modeling software were used tangentially in this study to model acquired data into t-T path solutions using two different inverse modeling approaches. Provided that QTQt and HeFTy run with differing algorithms (Bayesian for QTQt and Frequentist for HeFTy), running two separate functioning thermal model simulations provides advantages over just immediate replication of models, with the integration of fundamentally different statistical outputs from each software (described in detail by Vermeesch and Tian, 2014).

3.5.1 QTQt Modeling

To extract measured information recorded from thermochronologic dating into meaningful results, QTQt thermal modeling software (explained in detail by Gallagher et al., 2012) was used to simulate and extract non-unique t-T thermal model histories of all the collected samples in this study (Fig. 3.5). QTQt software's approach evaluates thermal history scenarios on a basis of "likeliness" with no regard to impossible circumstances and quality control of data, rendering geologic constraints ineffective. QTQt is formulated using a Bayesian statistical framework that runs on a MCMC (Markov chain Monte Carlo) sampling approach, which allows thermal history constraints including kinetics, annealing, and diffusion to be treated as prior probability information. By running Bayesian MCMC thermal modeling, the number of t-T path outputs are inferred from data instead of being

specified in advanced. Model parameters are sampled, the appropriate forward problems are solved for a given thermal history and some measure of fit is calculated for each data type. This process is repeated many times and the outcome is a collection of acceptable thermal history models, which acceptable can be quantified in terms of P-value probability.
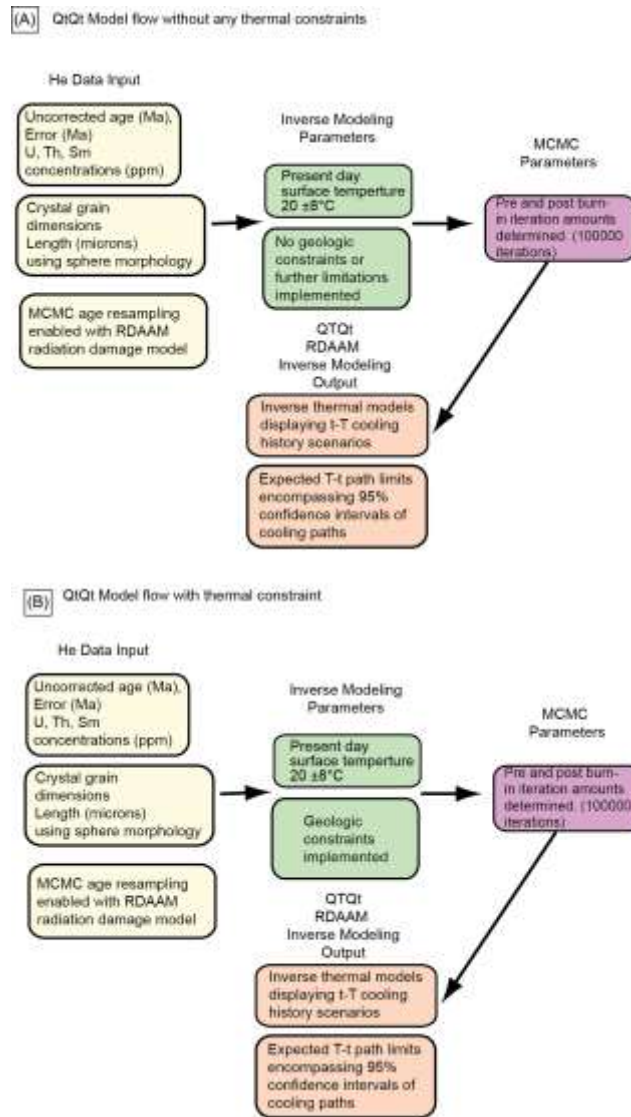
Figure 3.5: QTQt Model flow chart illustrating the thermal history modeling process applied in this study. (A) QTQt thermal history model flow chart input data inverse modeling parameters including thermal history constraints, and MCMC parameters, and output data. (B) QTQt thermal history model flow chart for QTQt models with input data without any constraints, inverse modeling parameters including thermal history constraints, and MCMC parameters, and output data.

In greater detail, the process MCMC is an iterative sampling approach to modeling in which the first part of the series, called the burn-in phase, consists of initial exploration of the model space. After the first series of runs, the burn-in phase results are discarded. The second part of the series, called the post-burn-in phase, is used to approximate the posterior distribution for the model parameters. In MCMC simulation, two models are a given iteration, a current model, and a proposed model. The model is generated by randomly perturbing the current model numerous iterations, with the first model being drawn randomly from the prior. At each iteration, either the proposed model is replaced with the current model, or the current model rejects the proposed model. The current model is collected at each iteration of this process and used as an approximation of the posterior distribution (summarized from Gavillot et al., 2018).

In this study, a minimalist approach to modeling is taken to impose the least amount of interference to simulations as possible, allowing the Bayesian Markov Monte Carlo Chain algorithm to judge likeliness of thermal histories from solely provided data. Given, imposed parameters included model limitations of present day surface temperature $20 \pm 8°C$ (Gondar data from Abebe, 2017) and the calibration of RDAAM (Radiation Damage Accumulation and Annealing Model) modeling to measured grain characteristics Flowers et al., 2009). Geologic constraints were not imposed in given appropriate models to best ensure models are resultant and independent of solely reflecting input constraints. With the input of measured (U-Th)/He data and corrected ages with minor error into QTQt data files, the resampling of cooling ages was allowed to ensure that the uncertainties in the observation are preserved in the predictive model, such as kinetics (Gallagher, 2012). Regarding iterations, 100,000 pre- and post-burn in phase iterations were set.

Using QTQt, (U-Th)/He ages for individual grain are modeled based on "likeliness" in decreasing order of probability of possible thermal history scenarios. Since QTQt generates results regardless of impossible circumstances, thermal constraints were not used for QTQt thermal history models. Models are presented as max mode t-T model option in QTQt that shows the distribution of all t-T paths, and the expected t-T history model with a swath that acts as the boundary of 95% confidence interval of t-T paths. The color grid outlines model space with hotter colors indicating higher relative probability of generated t-T paths.

3.5.2 HeFTy Modeling using Thermal History Constraints

HeFTy inverse modeling software (Ketcham, 2005), was also used as a tool to investigate and model a sample's time temperature histories with respect to geologic constraints and crystal characteristics (Fig. 3.6). HeFTy modeling is based on a frequentist statistical approach, which entails producing non-unique t-T history solutions accepted and rejected by their probability, expressed in P-values >0.05 and >0.5, marked as green being acceptable and purple being good. The evaluation method of data is effective for evaluating the probability of thermal histories that contain complex geologic phenomena impossible for software to consistently reproduce such as unconformities. In essence, HeFTy models use a frequentist statistics approach that produces quality-controlled thermal model solutions (Vermeesch and Tian, 2014).

HeFTy Model flow with thermal constraints

Model Inputs

Radioacive isotope
concentrations
U, Th, Sm, and He (ppm)

Crystal grain
dimensions
length (microns)
using spherical morphology

Measured
cooling age (Ma)
with error (Ma)

Present Day surface
temperature 20 ±8°C
calibrated with
with 10000 simulations
for inverse modeling

Speculated geologic constraints
developed from literature
and field data

RDAAM
Inverse Thermal Modeling
with HeFTy

Output

Thermal history models
displaying probable outcomes
with respect geologic
constraint accuracy

Quality controlled
t-T paths characterized
with varying degrees of
P-value acceptance

Figure 3.6: HeFTy thermal history model flow chart illustrating input thermochronologic data and thermal constraints and output data.

With the implementation of thermochronology data in to HeFTy (Flowers et al., 2009) model calibrations of alpha ejection redistribution was implemented on all samples. Model constraints (the apparent black boxes which t-T paths are confined to travel in t-T space) were primarily derived from a combination published literature, and field-based geologic analysis, and sensitivity testing of HeFTy parameters. With each sample, three main constraints were used (Table 3), documented, and outlined for replication purposes in the appendix. Regarding the starting point for all samples, initial cooling was referenced from Mock et al. (1999) geochronological analysis of basement rock across Ethiopia.

Leaving generous breathing room for uncertainty, the initial constraint imposed encompassed a range from 100-400°C during the time interval of 500-600 Ma across all samples modeled in HeFTy. The most important and relevant constraint input to HeFTy for this study was the thermal episode of flood basalt volcanism ~30 Ma (Hofmann et al., 1997). The flood basalt thickness ranges from 500-1000 m within the Tekeze River Basin area (Gani, 2015), and overly Mesozoic sedimentary rocks and basement rocks that contain the samples in this study. Geothermal gradients were constrained to a conservative average of 25°C/km, only encompassing the possibility of a speculative increase of temperature ranges due to mantle plume activity and volcanism, 25°C/km-35°C/km, during the 31-29 Ma basalt reheating constraint (Pik et al., 2003). The absence of Mesozoic rocks potentially eroding before volcanic rock emplacement is not disregarded, with a range of an additional possible 500 m of sedimentary cover on top of what is presently observed preceding basalt eruption. Considering the difference in elevation between each basement sample collected, overburden amounts were adjusted to include the vertical distance across each sample. Constraints also take into account the possibility of an additional 200 m of basement observed overlying the shallowest sample. The appearance of the flood basalt constraint are two boxes in t-T space, with one ranging 34-31 Ma, and another 31-29 Ma. The boxes were adjusted to accommodate temperature changes due to overburden amounts, with geothermal gradient 25°C/km before the eruption (34-31 Ma), and 25-35°C/km during the short eruption interval (31-29 Ma) (Hofmann et al., 1997). The conclusion of all HeFTy models is similarly bound to the same present-day temperature range as QTQt (Abebe, 2017).

4. RESULTS

A total of four Neoproterozoic Basement rock samples were collected along a vertical profile of the Tekeze River Canyon on the Ethiopian Plateau (Fig. 3.1). This study obtained a total of 16 individual apatite grains for (U-Th)/He and Fission-Track thermochronologic dating.

4.1 Results From Apatite (U-Th)/He Dating

Four grains were dated from each rock sample where the single-grain Ft corrected ages range from 207-12 Ma and [eU] range from 5-30 ppm (Table 1). The youngest sample E-35-17 was collected at the lowest elevation of 953 m yielded apatite (U-Th)/He cooling ages range between 12-35 Ma and grain radius of 37-39 µm. Sample E-38-17, collected at 1255 m elevation, yielded ages range from 33-107 Ma and grain radius range between 55-73 µm. In sample E-40-17, which was collected at 1446 m elevation, ages range between 26-207 Ma with grain radius range between 35-47 µm. The highest elevation sample E-43-17 yielded ages of 80-154 Ma with grain radius ranging between 28-37 µm.

To explore potential causes of spread among single-grain cooling ages, relationships among cooling ages, [eU] and r were explored (Fig. 4.1), as standard practice in thermochronologic studies using (U-Th)/He dating. In the age-elevation plot, a general weak positive correlation is observed with an R-squared value of 0.38 between the elevation and the single-grain (U-Th)/He ages of the apatite minerals. A slight deviation from this positive trend exists within the ages of E-40-17, which yield the most significant range of ages (26-207 Ma).

Table 1: Results of AHe data. Measured Summary of apatite (U-Th)/He cooling age thermochronologic dating and grain data. Elevation of each sample are in meters above sea level; r: derived grain radius assuming a spherical morphology; L: measured grain length; ^{238}U: measured Uranium isotope (parts per million); ^{232}Th: measured Thorium isotope (parts per million); ^{147}Sm: measured Samarium isotope (parts per million); ^{4}He: measured Helium isotope (moles); FT: alpha recoil ejection correction factor; Raw Age: uncorrected (U-Th)/He cooling age (Ma),); Corrected Age: alpha-recoil corrected (U-Th)/He ages (Ma); 1σ: propagated relative standard error (Ma).

Sample	Elevation (m)	r (μm)	L (μm)	^{238}U (ppm)	^{232}Th (ppm)	^{147}Sm (ppm)	eU (ppm)	^{4}He (moles)	Mean FT	Raw Age (Ma)	Corrected Age (Ma)	1σ (Ma)
E-35-002	953	39.70	113.94	3.36	7.38	44.49	5.11	5.01E-16	0.63	11.32	17.87	1.18
E-35-003	953	36.31	119.66	5.14	10.09	58.04	7.55	4.30E-16	0.62	7.55	12.27	1.02
E-35-004	953	34.82	102.69	4.22	6.12	16.96	5.69	6.81E-16	0.60	20.87	35.04	2.58
E-35-005	953	37.33	123.35	5.55	5.87	50.67	6.97	5.23E-16	0.63	9.16	14.54	0.87
E-38-001	1255	73.36	239.62	10.30	13.00	28.59	13.43	3.56E-14	0.80	44.90	56.17	0.81
E-38-002	1255	55.75	207.15	23.42	30.74	22.67	30.82	7.25E-14	0.75	80.44	107.73	1.59
E-38-003	1255	65.30	219.22	7.70	11.61	9.27	10.48	1.48E-14	0.78	33.41	43.03	0.79
E-38-005	1255	63.82	218.72	2.91	4.96	16.32	4.09	4.42E-15	0.77	26.08	33.79	0.70
E-40-001	1446	47.31	157.86	11.15	15.56	26.70	14.88	1.82E-14	0.70	75.67	108.19	1.79
E-40-002	1446	46.79	147.06	14.53	34.14	16.48	22.66	4.75E-14	0.69	142.62	207.09	3.06
E-40-003	1446	35.87	137.42	15.55	26.19	29.43	21.82	1.20E-14	0.62	68.23	109.60	1.91
E-40-004	1446	43.54	141.23	7.17	11.54	32.55	9.94	2.22E-15	0.67	18.08	26.86	1.15
E-43-001	1765	31.31	127.43	6.52	17.43	159.71	10.66	3.55E-15	0.57	52.67	91.72	3.74
E-43-002	1765	37.72	159.53	6.87	20.24	154.45	11.68	6.81E-15	0.64	51.35	80.36	1.88
E-43-003	1765	28.24	123.88	7.39	12.48	158.98	10.38	4.40E-15	0.55	84.38	154.66	5.84
E-43-005	1765	34.82	115.50	8.80	8.51	119.72	10.87	4.09E-15	0.61	54.67	89.98	2.62

A lack of correlation is effectively defined between the cooling age and grain radius (Figs. 4.1B, C). The cooling ages display a positive-slope relationship with [eU] (Figs. 4.1E, F) with the strongest correlation exists in samples E-40-17 (R-squared value 0.99) and E-38-17 (R-squared value 0.72) (Figs.4.1E, F). This positive correlation between [eU] and cooling ages suggests these samples have undergone radiation damage effect.

An analysis of thin section petrographic study of all samples was conducted to investigate the presence of adjacent bad neighbor effect of any apatite, zircon, and monazite that can inject He to the apatite grains. None of the sample show any of the radiogenic bad neighbor to apatite in the thin sections (Figs. 3.3, 3.4).
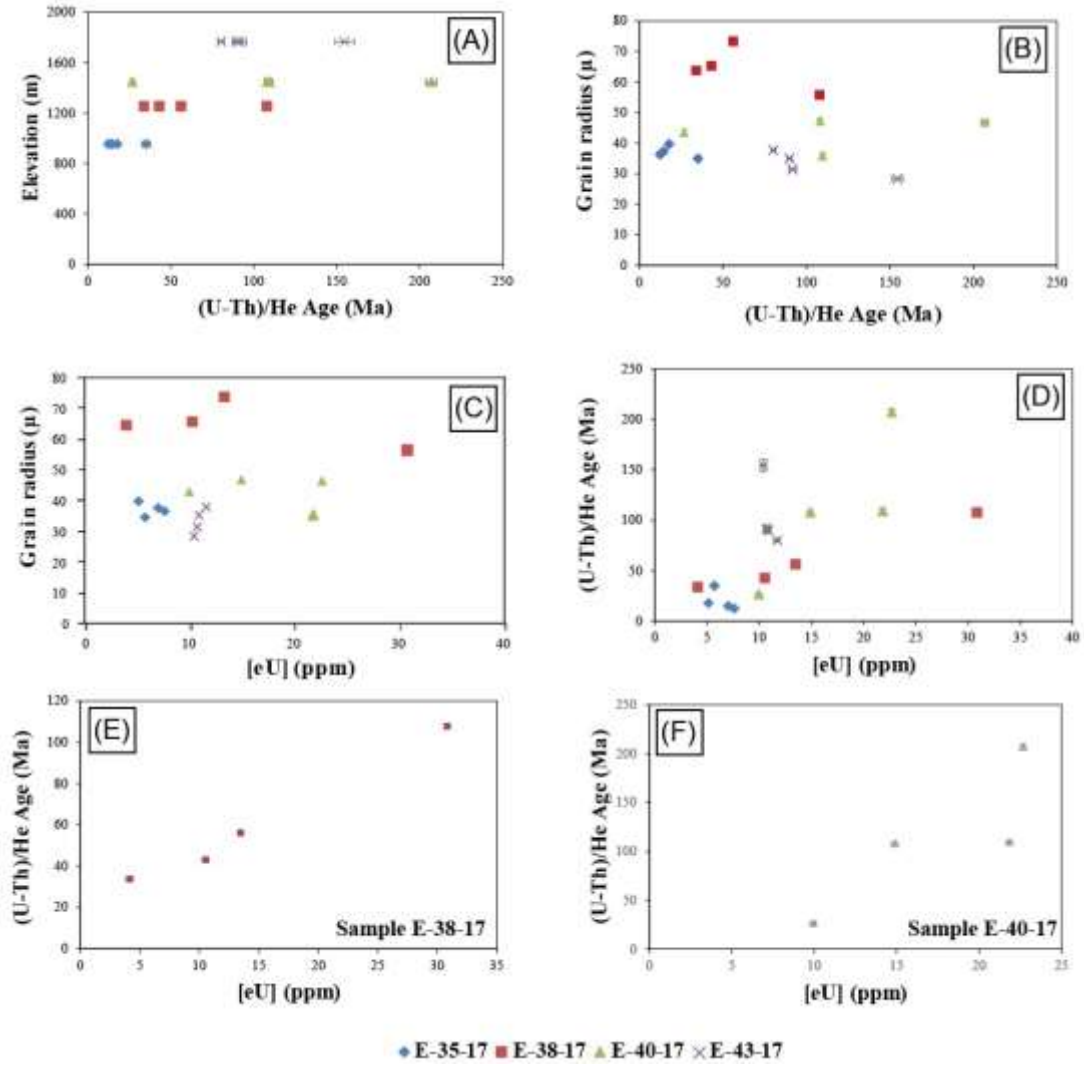
Figure 4.1: Apatite (U-Th)/He (AHe) thermochronologic data plots. (A) Age vs. elevation plot, displaying the positive relationship with cooling age and elevation of samples, with the presence of variability being more apparent in the older samples. (B) Age vs. grain radius plot, displaying no correlative relationship among samples. (C) [eU] vs. grain radius, showing a lack of relationship. (D) [eU] vs. age plot showing an overall relationship suggestive of radiation damage.(E) and (F) show [eU] vs. age plot of E-38-17 and E-40-17 samples, respectively, with strong presence of radiation damage E-38-17, and (D): E-40-17.

4.2 Results From Apatite Fission-Track Dating

The results with apatite fission-track cooling ages, length data and standards are summarized in Table 2. From the three Neoproterozoic basement samples (E-35-17, E-38-17, and E-43-17), ages are reported as 1-Sigma uncertainty of pooled fission-track ages.

Table 2: Results of AFT data. Summary of apatite fission-track data. Three apatite fission-track samples are reported. Elevation of each sample are in meters above sea level; Counted Fission-Tracks are the total number of fission-tracks for each sample; Spots indicate fixed points at which Uranium was measured; Pooled ages are the mean of the total Fission-Track ages (Ma) for each sample; Mean U-Pb Age is the mean of total measured U-Pb ages from each sample. Error is reported as ± Ma from measured Cl (Chlorine) concentration.

Sample	Elevation (m)	Counted Fission-Tracks	Spots	Pooled Age (Ma)	95%-CI (Ma)	95%+CI (Ma)	U (ppm)	Mean U-Pb Age (Ma)
E-35-17	953	646	39	189.26	59.69	80.44	16.47	637.79
E-38-17	1255	2351	25	353.62	29.69	32.34	13.68	645.71
E-43-17	1765	1290	25	326.71	29.00	31.75	7.45	658.67

Across all samples, overall age-elevation relationship is lacking (Fig. 4.2) emblematic as more strongly reflecting the AHe variation. E-35-17 produced a spread of ages pooling at 189 Ma with a mean Dpar of 1.80. E-38-17 yielded fission-track ages, which pooled at 353 Ma, and a mean Dpar of 1.88. E-43-17 contained a spread of track ages pooling at 326 Ma and a mean Dpar of 1.79. All fission-track ages are older (>154 Ma) than the (U-Th)/He ages, which is logically consistent with the differing thermochronometer closure temperatures. This trend of cooling age may indicate progressively older cooling age towards the top/north. The mean track-length of these three samples were plotted, where each displayed unimodal track-length distribution (Fig. 4.2). Mean track length distributions for samples E-35-17, E-38-17, and E-43-17 reside at 12.29 µm, 11.79 µm, and 12.17 µm, respectively. The attributing distributions of the track lengths reside modestly normal, with the majority of lengths in the distributions falling below the 15 µm track length threshold Such distribution, as characterized by Donelick et al. (2005), is indicative of samples that underwent temperature driven annealing well after formation, characterizing possibilities more recent scenarios of rapid cooling.
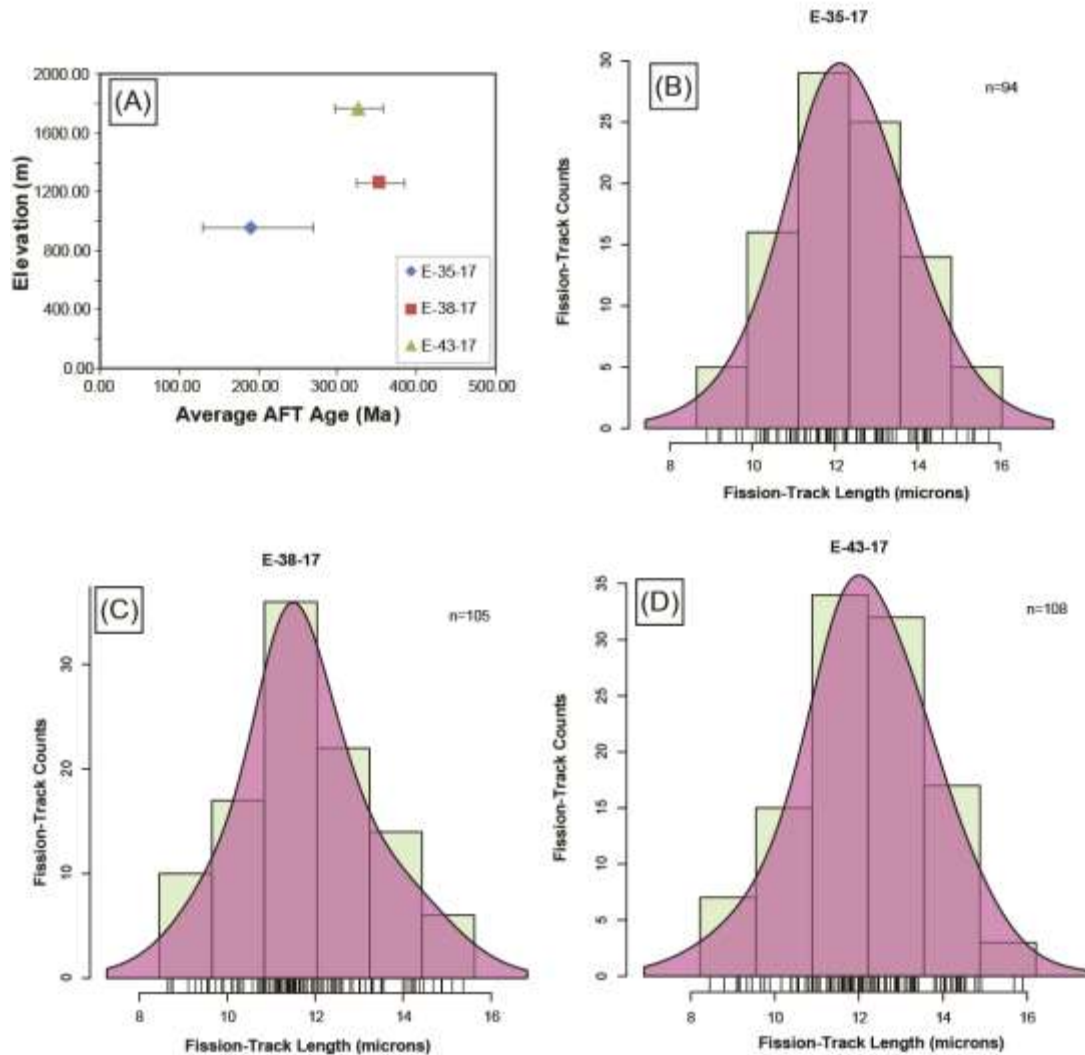
Figure 4.2: Apatite Fission Track (AFT) thermochronologic data plots. (A) Age vs. elevation, with an observable lack of relationship among the fission-track ages across elevation. (B), (C), and (D) display the fission-track length histograms of sample E-35-17, E-38-17 and E-43-17, respectively, with the distributions shaped moderately normal where the most common sizes having more counts (n).

4.3. Results from Thermal History Models

Although each sample shows cooling ages, the single-grain t-T models for each sample are created to constrain their time-temperature paths. Single-grain QTQt models for E-43-17 display general young cooling history (Late Cretaceous ranges from ca. 106-

62 Ma) than their AHe cooling ages (Fig. 4.3). All the grains show rapid cooling during this time to ~75°C (Fig. 4.3). When using the heating event constraints of 30 Ma flood basalt event, the individual grain model shows similar trend of Late Cretaceous rapid cooling, which is followed by slow cooling and then another rapid cooling event ~28 Ma that continued to the present day (Fig. 4.3). The AFT QTQt t-T models for E-40-17 displays rapid cooling ~45 Ma (Fig. 4.4). Thermal history models were constructed for both AHe and AFT ages of individual grain of E-43-17 using HeFTy software with thermal constraints. None of these HeFTy models show observable rapid cooling event trends post-30 Ma.

The individual-grain QTQt models for sample E-40-17 show a similar trend of rapid cooling during Mid-Late Cretaceous (Fig. 4.4). Grain E-40-004 shows rapid cooling event around 23 Ma (Fig. 4.4D). When using the 30 Ma flood basalt constraint, the individual grain models of E-40-001, E-40-002 and E-40-003 show the Cretaceous rapid cooling event that continued to the present day (Figs. 4.4F, G, H). Similar to sample E-43-17, thermal history models using constraints in HeFTy software were also constructed for both AHe and AFT ages of individual grain of E-40-17, which show no significant rapid cooling paths post 30 Ma.

Table 3: Geologic constraints used for thermal history models in this study. Constraints were derived from a combination of acquired field data and literature. For QTQt models, only the ~30 Ma trap flood basalt thermal resetting constraint was used. With In HeFTy models, all constraints listed in the table were implemented.

Sample	Precambrian Time (Ma)	Precambrian (T)	Mesozoic (Ma)	Mesozoic (T)	Pre-Basalt Time (Ma)	Pre Basalt (T)	Basalt (Ma)	Basalt (T)
E-35-17	600-500	100-500	130-80	45.5-90	34-31	45.5-58	31-29	55-90.5
E-38-17	600-500	100-500	130-80	37.5-90	34-31	37.5-50	31-29	47.5-79.5
E-40-17	600-500	100-500	130-80	32.5-45	34-31	32.5-45	31-29	42.5-72.5
E-43-17	600-500	100-500	130-80	25-90	34-31	25-37.5	31-29	35-62.5
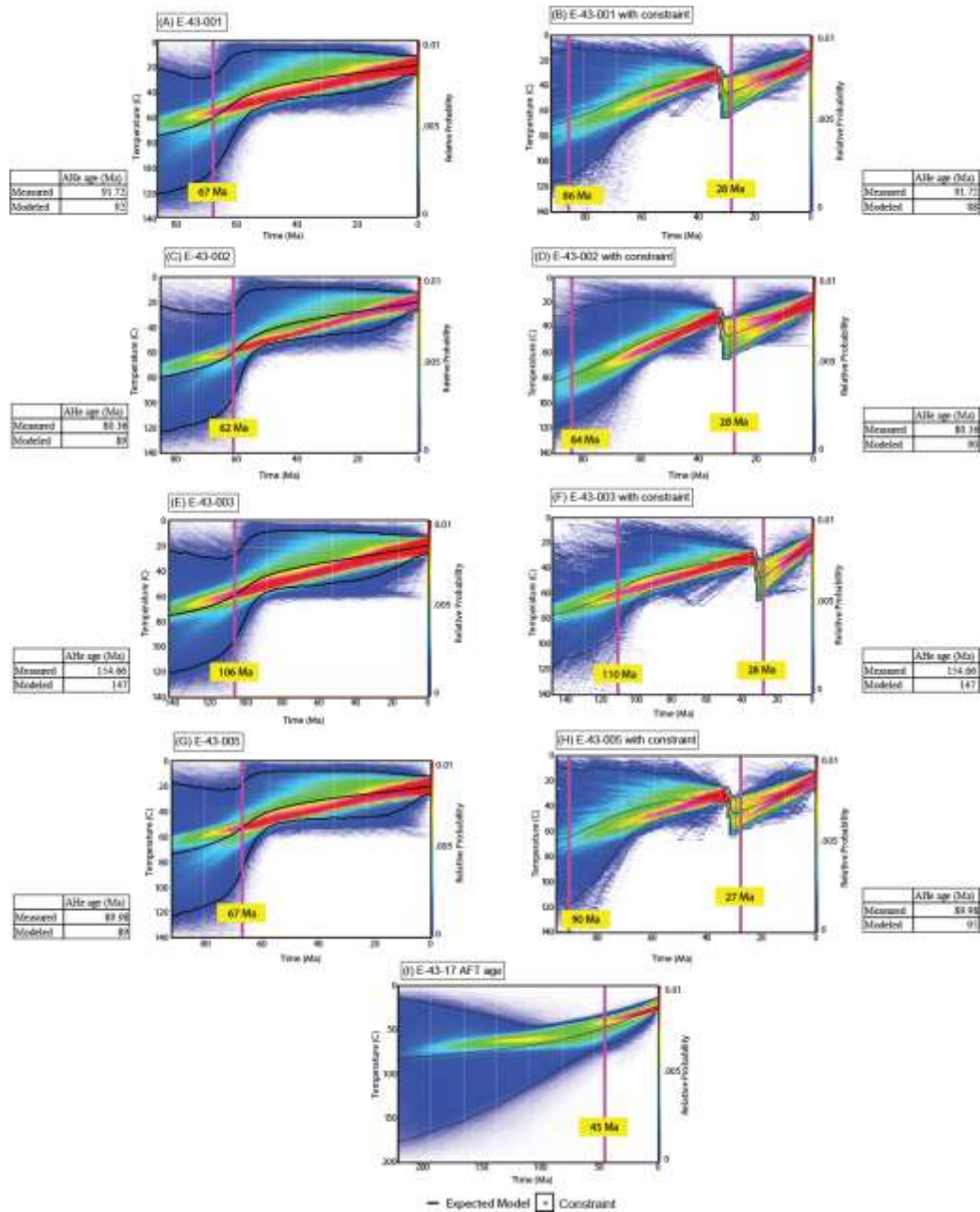
Figure 4.3: E-43-17 thermal models. (U-Th)/He thermal history models results from QTQt for grains E-43-01, E-43-002, E-43-003, and E-43-005 of sample E-43-17 with measured and modeled AHe ages. Figures (A), (C), (E) and (G) show models that are generated without using any constraints. These models display a rapid cooling phase in the Late Cretaceous (62-67 Ma) except model in (E) that represent an outlier with an older cooling event at 106 Ma. Figures (B), (D), (F) and (H) show models that are generated using thermal constraints. These models mostly display observable rapid cooling in the Late Cretaceous (84-90 Ma) with the addition of a Late Oligocene rapid cooling (27-28 Ma) following the simulated reheating constraint. (I) fission-track thermal history model results from QTQt for sample E-43-17 where rapid cooling is observable at 45 Ma.

38
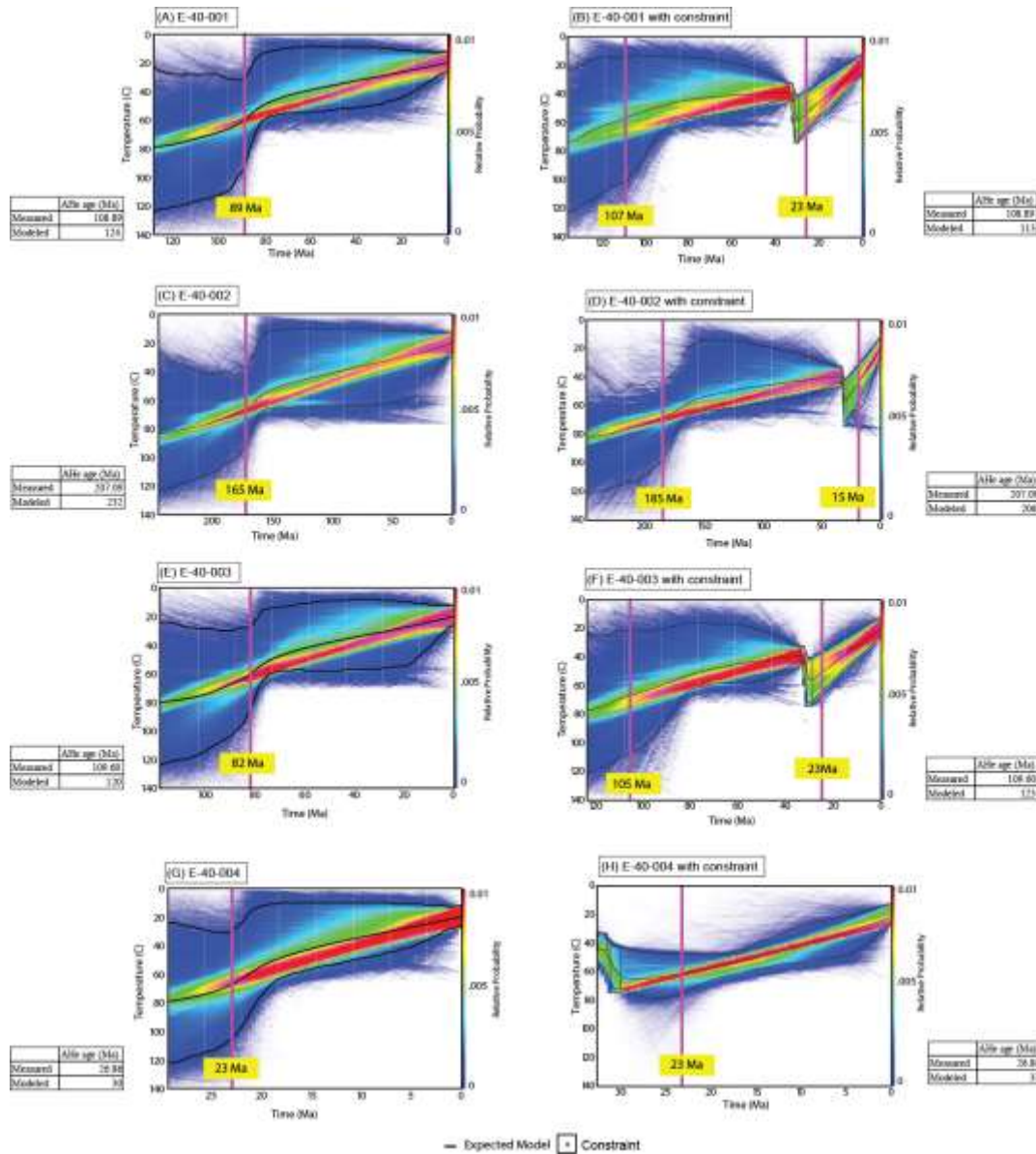
Figure 4.4: E-40-17 thermal models. (U-Th)/He thermal history models results from QTQt for grains E-40-01, E-40-002, E-40-003, and E-40-004 of sample E-40-17 with measured and modeled AHe ages. Figures (A), (C), (E) and (G) show models that are generated without using any constraints. These models display a rapid cooling phase in the Mid-Late Cretaceous (82-165 Ma) with the youngest rapid cooling at 23 Ma in (G). Figures (B), (D), (F) and (H) show models that are generated using thermal constraints. These models mostly display observable rapid cooling in the Mid-Late Cretaceous (105-185 Ma) with the addition of a Late Oligocene rapid cooling (23 Ma) due to the simulated reheating constraint, which is followed by a young rapid cooling ~15 Ma.

The individual-grain E-38-002 QTQt model for sample E-38-17 show a similar trend of rapid cooling during Late Cretaceous (Fig. 4.5B). When using constraints, this grain shows two additional rapid cooling events ~28 Ma and ~10 Ma. Grain E-38-001 and E-38-003 show Paleocene-Eocene rapid cooling events in both scenarios of using constraints and without any constraints, while E-38-005 show rapid cooling event around 23 Ma in such similar scenarios (Figs. 4.5A, C, D). All of the grain models show 28 Ma rapid cooling when using the 30 Ma flood basalt constraint (Fig. 4.5). The t-T models from AFT age for E-38-17 displays rapid cooling at 45 Ma (Fig. 4.5I). With sample E-38-17, no clear discernable rapid cooling relationship post 30 Ma is evident for any of the grain models using AHe and AFT ages in HeFTy.

For sample E-35-17, the thermal history modeling results of each single-grain apatite E-35-002, E-35-003 and E-35-005 show young cooling post-30 Ma (Figs. 4.6A, B, D). These models indicate rapid cooling from 15 Ma to as young as 10 Ma after the 30 Ma flood basalt eruption (Fig. 4.6), when most of the incision happened, likely associated with base level perturbations. Cooling distribution after the last 10 Ma to the Present time remain unclear due to the thermal history model directional uncertainties. Only grain E-35-004 show 28 Ma rapid cooling like the other sample grains (Fig. 4.6C). Expected t-T models from AFT age for E-35-17 displays older cooling profiles (45 Ma) (Fig. 4.6E). From the HeFTy thermal models, results were able to be successfully generated with applied thermal history constraints. From the thermal models, the t-T history paths most clearly dictated rapid cooling after being thermally reset post 30 Ma for E-35-17, the sample with the youngest cooling ages. Individual grain models for E-35-17 grain samples bared strong

resemblance among the distribution of "good fit" simulated paths. For example, sample E-35-003 shows a rapid cooling event ~12 Ma, so as sample E-35-005 (Figs. 4.6.F, G).
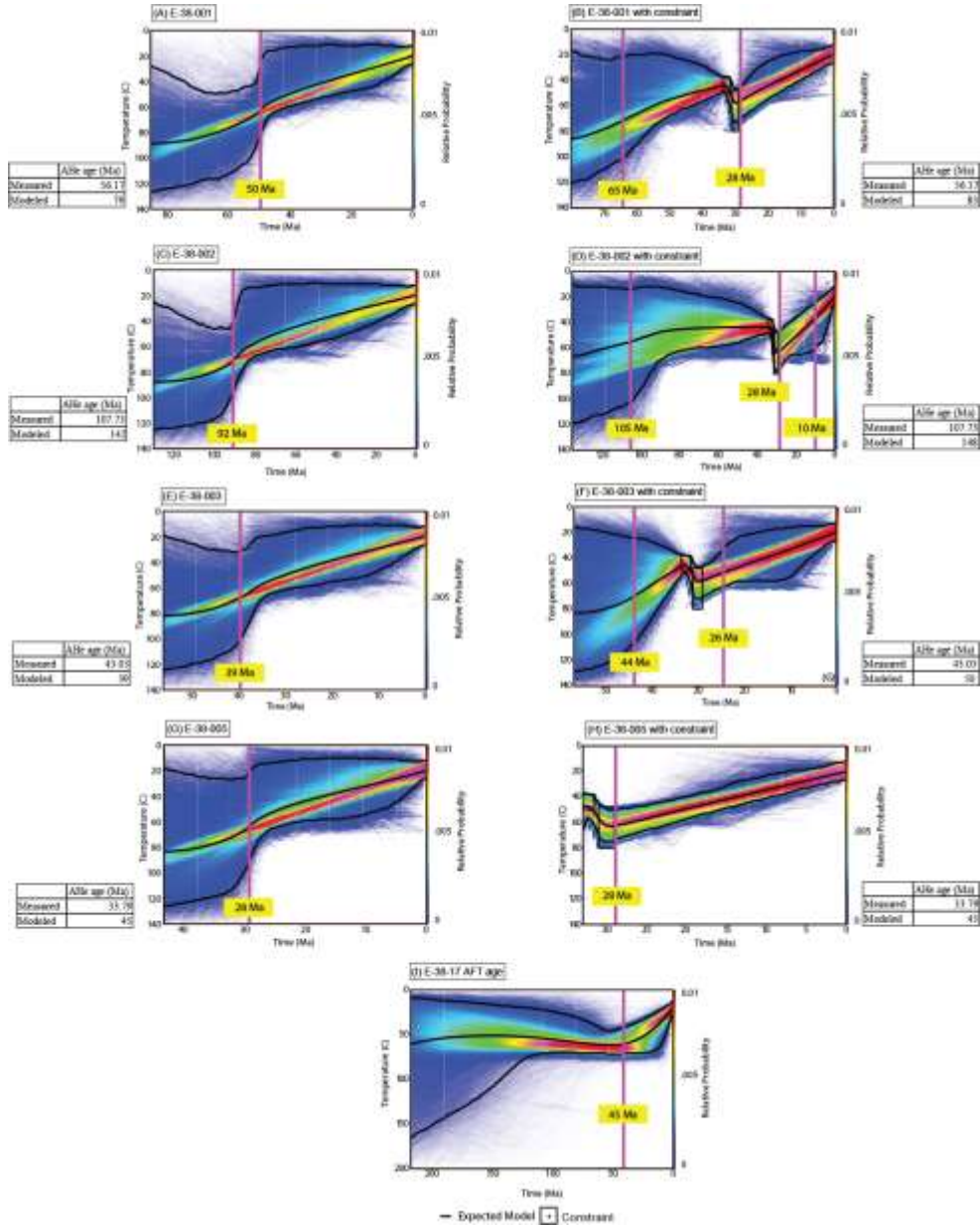

Figure 4.5: E-38-17 thermal models. (U-Th)/He thermal history models results from QTQt for grains E-38-01, E-38-002, E-38-003, and E-38-005 of sample E-38-17 with measured and modeled AHe ages. Model in (A) displays the onset of rapid cooling at 50 Ma evident from the inflection and tightening of generated t-T paths. Model in (C) shows rapid cooling

at 92 Ma, in (E) 39 Ma and in (G), 28 Ma. Figures (B), (D), (F) and (H) show models that are generated using thermal constraints. Model (B) experiences the first initial phase of observable rapid cooling at 65 Ma and 28 Ma after the most recent simulated reheating constraint. Model (D) shows an initial rapid cooling at 105 Ma followed by rapid cooling at 28 Ma and 10 Ma. Model in (F) experiences its first phase of rapid cooling at 44 Ma followed by another rapid cooling at 26 Ma after the reheating simulation. Model in (H) shows a rapid cooling at 28 Ma. (I) fission-track thermal history model results from QTQt for sample E-38-17 where rapid cooling is observable at 45 Ma.
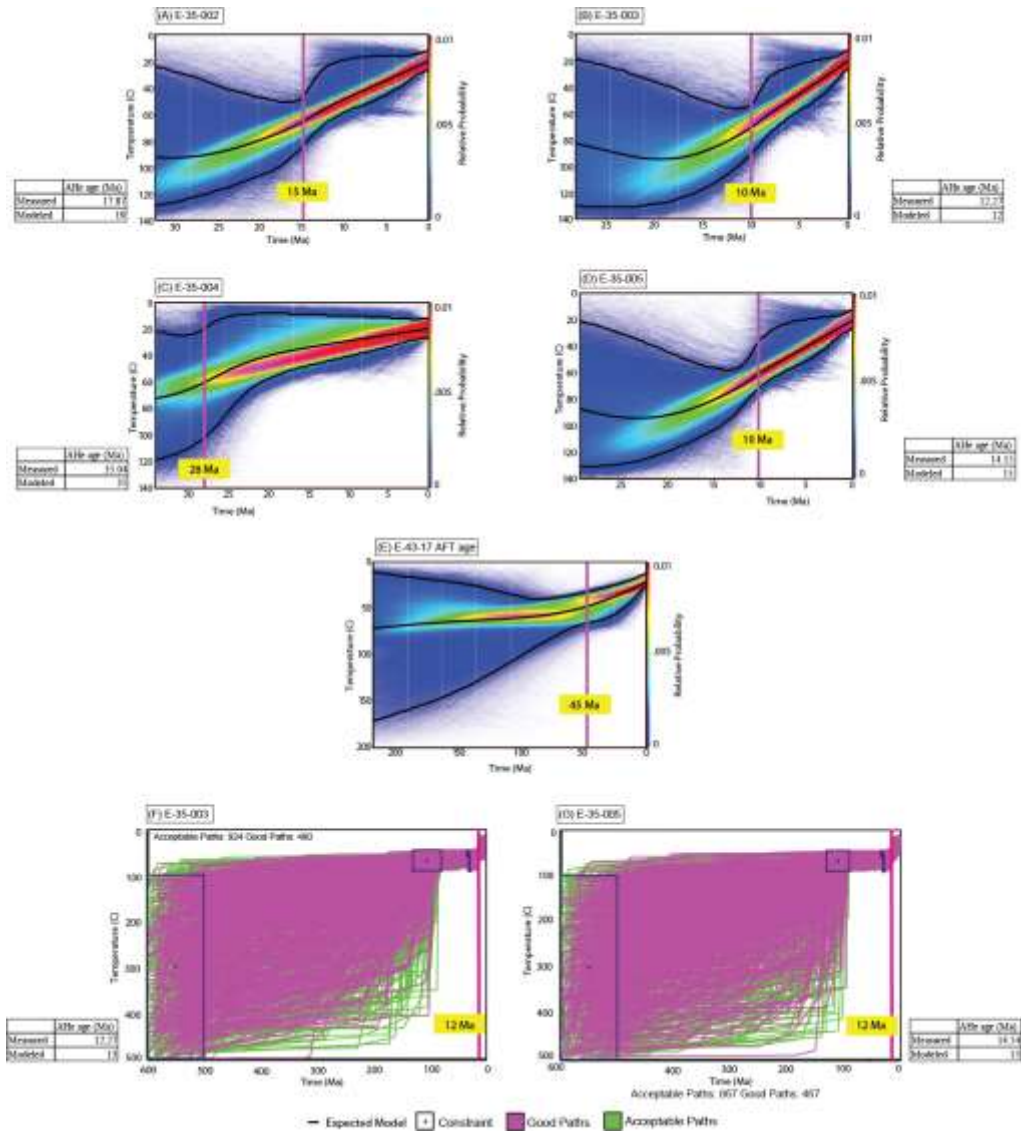
Figure 4.6: E-35-17 thermal models. (U-Th)/He thermal history models results from QTQt for grains E-35-02, E-35-003, E-35-004, and E-35-005 of sample E-35-17 with measured and modeled AHe ages. Figures (A), (B), (C) and (D) shows models that are generated

using any constraints. Each of these models display rapid cooling as young as 15 and 10 Ma in the absence of applying the reheating constraint. Model (A) displays rapid cooling occurring at 15 Ma, while (B) experiences observable rapid cooling 10 Ma. (C) differs from the other modeled grains of this sample with an older rapid cooling transition at 28 Ma. (D) models a faster cooling transition at 10 Ma. (E) fission-track thermal history models results from QTQt that displays the most prominent observable rapid cooling transition at 45 Ma. (F) and (G) (U-Th)/He thermal history models results from QTQt for grains E-35-003 and E-35-005 generated with constraints. Model (F) displays its most prominent rapid cooling at 12 Ma, while (G) modeled a rapid cooling transition at 12 Ma.

Batch models or sample models (includes all grains) of each sample illustrate a reasonable t-T history along the vertical profile from which these samples are collected (Fig. 4.7). These batch model shows that the lowest elevation sample E-43-17 underwent the older cooling history (Fig. 4.7D). It cooled during the Cretaceous time (~66 Ma) and did not affected by any burial resetting. Samples E-40-17 and E-38-17 display slightly different thermal history (Figs. 4.7B, C). E-40-17 shows a combination of rapid cooling and slow cooling (Fig. 4.7C), which is probably due to partial resetting as a result of burial. Sample E-38-17 also shows partial resetting and rapid cooling event ~33 Ma, thus implying cooling related to incision (Fig. 4.7B). Since this sample is not fully reset, it does not show a younger cooling history. Sample E-35-17 recorded the youngest cooling ages, which is also the lowest elevation sample and shows full resetting record in its young cooling ages as young as 12 Ma (Fig. 4.7A). This is also reflected in the AFT and AHe batch models of the E-35-17 sample (Fig. 4.7).

Figure	Measured AHe age (Ma)	Modeled AHe age (Ma)
4.7 (A)	17.87; 12.27; 13.04; 14.54	17; 17; 16; 18
4.7 (B)	36.17; 107.73; 43.03; 33.79	136; 138; 126; 126
4.7 (C)	308.89; 207.09; 109.60; 26.86	207; 265; 202; 202
4.7 (D)	91.72; 80.36; 154.66; 89.98	66; 66; 66; 66
4.7 (E)	36.17; 107.73; 43.03; 33.79	139; 139; 139; 139
4.7 (F)	308.89; 207.09; 109.60; 26.86	200; 200; 200; 200
4.7 (G)	91.72; 80.36; 154.66; 89.98	69; 69; 69; 69
4.7 (H)	29.18	20
4.7 (I)	19.60	28
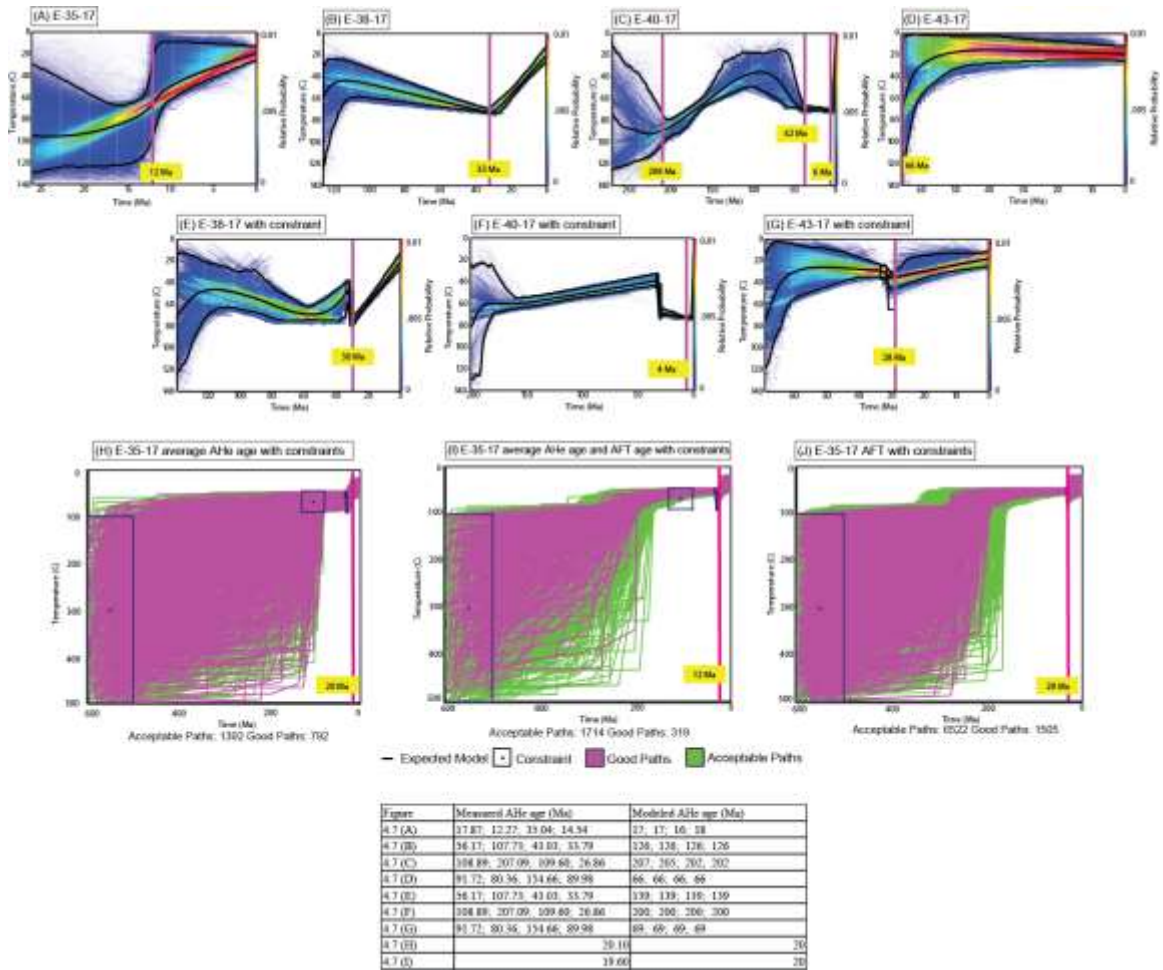
Figure 4.7: Group thermal models. Figures (A), (B), (C) and (D) show (U-Th)/He thermal history models results from QTQt for E-43-17, E-40-17, E-38-17, and E-35-17 with measured and modeled ages (created with the aggregate of all grains measured data in each sample) that are generated without thermal constraints. Model (A) displays rapid cooling at 12 Ma. While (B) shows cooling at 33 Ma. (C), concurrent with the wide range of cooling ages, shows rapid cooling at three distinct periods 208 Ma, 42 Ma, and 6 Ma. (D) shows cooling at 66 Ma. Figures (E), (F) and (G) show (U-Th)/He thermal history models results from QTQt generated with thermal constraints. (E) displays rapid cooling 30 Ma, while (F) cools later at 4 Ma. With constraints, (G) experienced a transition to rapid cooling 28 Ma. (H) (U-Th)/He thermal history models results from HeFTy for sample E-35-17 generated with the average measured AHe data of sample E-35-17 with constraints. This model shows an onset of rapid cooling at 20 Ma, while (I) cools at 12 Ma (I) fission-track thermal history models results from HeFTy generated with average E-35-17 measured AHe data, fission-track data, and constraints. (J) fission-track thermal history models results from HeFTy generated with constraints, which shows a cooling transition at 28 Ma.

5. DISCUSSION

5.1 Correlation between Thermochronologic Results and Contributing Parameters

AHe data obtained from the Neoproterozoic basement rocks display a range of ages indicating a complex thermal history that the study area experienced. Several factors can contribute to the age variation as discussed below. From evaluation of measured and observed data, relationships suggest that sample E-35-17, the lowest elevation sample with the youngest cooling ages, displays the most strongly preserved rapid cooling events post 30 Ma relevant to this study, coupled with the least semblance of variability compared with the rest of our data.

Temperatures effect on the variation of helium diffusivity grain size, uranium zonation, and radiation damage can attribute to cooling age spread (Flowers and Kelley, 2011). Larger grains can prevent diffusion causing variation in closure temperatures (Reiners and Farley, 2001). However, no correlative relationship between grain size and age in the dataset was observed, showing a statistically insignificant R-squared value of 0.0001. In terms of diffusivity, the likely impeding factor causing spread among cooling age is the radiation damage related to [eU] content. Graphical relationships support [eU] has a strong positive correlation among E-38-17 (R-squared value 0.72) and E-40-17 (R-squared value 0.99), which are the samples with the largest spread among cooling ages in the data. SEM-BSE (Scanning Electron Microscopy-Backscattered Electron Imagery) was also used to evaluate [eU] zonation in grains, however, no zonation was observed, indicating that either BSE detector was not sufficient for zonation identification, or there was no eU zonation.

Further limiting factors known to contribute to age spread include the consequences of having He implantation (Fitzgerald et al., 2006; Spiegel et al., 2009) or inclusions within samples. Thin sections were observed to analyze possible instances of bad neighboring effects from nearby radiogenic crystals injecting helium into apatite grain. No bad neighbor was found in any samples. Micro-inclusions not visible when evaluating grains for dating can cause significant discrepancies in age with secondary runs in alpha particle mass spectroscopy producing irregularly high values (Vermeesch et al., 2007). Such questionable grains have been removed from our data during analyses.

The positive correlation observed in the age-elevation relationship among the samples suggests the rocks were not subsequently affected by faulting and igneous intrusions, indicating radiation damage was a stronger possibility for age dispersion. The samples experiencing the most significant variation of cooling ages were E-38-17 and E-40-17. Both contained positive correlations between [eU] and cooling age. Samples E-38-17 and E-40-17 displayed no relationship between [eU] and radius, or radius and age, suggesting the samples solely suffered radiation damage, a likely resultant from being partially reset, or sitting in the partial retention zone for an extended period of time. This observation was also found in data obtained by Bowden et al., (2018). No additional relationships were found between eU and radius, age and radius, or [eU] and age within E-35-17 and E-43-17.

With corrected cooling ages ranging between 51-84 Ma E-43-17 samples show a lack of evidence to support unequal helium diffusivity, bad neighbor injection, and zonation. Despite the lack of direct evidence for radiation damage, being the highest

elevation and shallowest sample E-43-17 was likely partially reset by increased overburden and burial during the 30 Ma flood basalts (Hofmann et al., 1997).

Combined with AHe data, fission-track data can also aid in revealing age spread of data (Flowers and Kelley. 2011). AFT data show the non-monotonic in the age-elevation relationship between E-35-17, E-38-17 and E-43-17. With the inconsistency of E-38-17 and E-43-17, overlap is experienced from measured ages at the 1-sigma uncertainty level, bearing resemblance with the dispersion of AHe data. This relationship suggests consistency where E-38-17 likely underwent partial resetting or was in the partial retention zone for a long period of time (Flowers and Kelley, 2011).

Additional insight of fission-tracks is evident from analysis of fission-track lengths. Freshly formed fission tracks measured close to 15 µm in length, if the length is less than 15 µm, it is assumed that temperature-driven annealing occurred after fission track formation (Donelick et al., 2005). Additionally, samples that underwent slow cooling, followed by rapid cooling to present day are characterized by shorter tracks (Donelick et al., 2005). If a sample underwent rapid cooling followed by a period of slow cooling that sample would be dominated by long tracks, which have not had the time to anneal. Across all three samples, mean track lengths reside at 12.28 µm, 11.79 µm, and 12.17 µm, suggestive of initial slow cooling during formation when grains experienced sufficient time to anneal before experiencing recent rapid cooling to present day. In context, this slow cooling preceded thermal reheating due to flood basalts overburden. Following reheating, the samples experienced rapid exhumation and cooling from incision.

5.2 Low-Temperature Thermal History and Geologic Implications of the Northwestern Ethiopian Plateau

In this study, t-T histories were simulated by employing a combined thermochronologic modeling software approach that integrates both QTQt and HeFTy to evaluate the thermal history of the thermochronologic data. Both intra-sample grain model as well as batch sample models that incorporate the aggregates of all grains in each sample are presented. Our modeling scheme provides advantages through the immediate replication of thermochronologic data tangentially into two separate formulated software (QTQt and HeFTy) with differing statistical approaches to modeling measured data inputs. HeFTy, input data were modeled with respect to known geologic constraints in which the goodness of fit between model predictions (constraints) and input data are tested in output models with probability based (P-value) quality controlled output models. QTQt contributed to our modeling methods by use of evaluating thermochronologic data with the least amount of interference to simulations as possible, using a bayesian statistical approach best reflects the quality of input data in contrast to the likeliness and reproducibility of data fitting into estimated geologic constraints with HeFTy.

To understand the implications of the geologic history generated from thermal history models, it was of utmost importance to understand the mechanisms by which the samples heated and cooled. It was also necessary to consider influences of burial related overburden and radiation damage effect stored in the cooing ages and thermal history models of each sample. Upon crystallization, Proterozoic to Early Paleozoic rocks heated in excess of ~500°C to metamorphose into greenschist facies (Mock et al., 1999). Following the initial event during the Paleozoic, limited information aside from AFT

thermal history models support long period of cooling likely attribute to the exhumation associated with the Gondwana rifting (Binks and Fairhead. 1992; Abbate et al., 2015). Western Ethiopia likely underwent an extended period of tectonic dormancy, characterized by the gradual cooling before plume emplacement and rifting.

With the presumption of a relative homogeneity of thermal flux in the study area, is assumed that thick flood basalts from the fissure eruption had rapidly buried the samples ~30 Ma. If the flood basalts had caused any burial related reheating to the topmost sample E-43-17, consequences of partial resetting would be more apparent in this sample, which is not the case. Each grain in this sample recorded older cooling ages. The AHe ages in this sample range between 80-154 Ma while the AFT age is 326 Ma. The partial resetting effect is most prevalent in lower samples, indicating the samples were sufficiently buried enough to prevent direct reheating from the burial of flood basalt. Sample E-38-17 and E-40-17 incorporate radiation damage, which indicates longer residence in the partial retention zone and is attribute to the burial related to the flood basalts ~30 Ma. The young age (12-35 Ma) of sample E-35-17 indicates that this sample had undergone burial related thermal resetting, similarly observed in Bowden (2018).

Each batch sample model displays a vertical gradation of burial related resetting effect within t-T history (Figs. 4.7A-J). These batch models show that the lowest elevation sample E-43-17 has older cooling ages from Cretaceous time (~66 Ma) rapid cooling events followed by 28 Ma rapid cooling (Figs. 4.7D, G). Therefore, this sample was not affected by any burial resetting. Samples E-40-17 and E-38-17 likely underwent partial resetting as a result of burial. Therefore, these two samples remained in the partial retention zone for longer time. E-40-17 shows an old Cretaceous rapid cooling followed by a slow

cooling and a very young rapid cooling event around 4-6 Ma (Figs. 4.7C, F), thus indicating later rapid cooling resultant of incision. Sample E-38-17 also shows partial resetting due to rapid cooling ~33 Ma (Figs. 4.7B, E). Because this sample experienced partial thermal resetting like sample E-40-17, it does not contain any younger cooling ages. Sample E-35-17 with the youngest cooling ages, shows complete thermal resetting record due to burial (Figs. 4.7A, H-J). The thermal history model of this sample shows ~12 Ma, rapid cooling, thus increased incision occurred on the Ethiopian Plateau (Fig. 4.7A). The AFT and AHe batch models of the E-35-17 sample both display similar trends of increase incision around 12 Ma (Fig. 4.7I). Therefore, E-35-17 being the sample containing youngest cooling ages, the smallest observed range of cooling age variation, and coupled with no evidence of radiation damage effects, is rendered most reasonable and best representative sample in our data for understanding the Cenozoic post-30 Ma incision history of the Tekeze River, and by proxy, the Ethiopian Plateau.

After experiencing the onset of domal uplift, the study area was overlain by flood basalts before the development of the present-day incised topography. After the flood basalt eruption, river incision began 30-20 Ma. Detailed analysis of the thermal history models of E-35-17 reveals most prominent cooling and subsequent incision characterized with the first rapid phase of cooling that started ~12 Ma, which is likely when increased river incision likely began to exhume the samples. This contrasts with the previous finding from Pik et al. (2003) study, with the presumption of a majority of incision having occurred between 29-25 Ma, with little to no change since initiation. The rapid incision required to have cooled samples rapidly is reflective
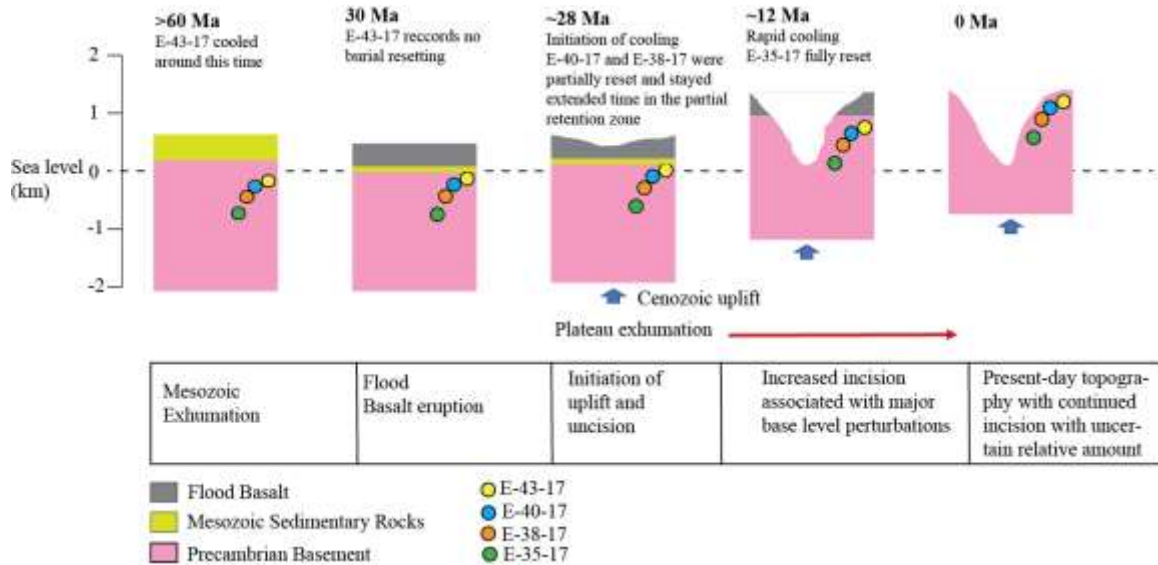
Figure 5.1: Block model diagram. Schematic block model displaying summarized conclusions of low-temperature thermal history of the Northwestern Ethiopian Plateau. From this study, it is interpreted that initiation of uplift and incision began after the flood basalt eruption ~28 Ma. Incision continued, transitioned to increased rates ~12 Ma in agreement with the 100m/Ma rate of incision observed from Gani (2015). Around 6 Ma, a second phase is identified, with the presumption of incision to continue until the present-day, with no clear discernable relationship among relative rates from models.

of base level change likely attribute to the Ethiopian Plateau uplift. While not being the sole mechanism, the mantle plume-related domal uplift of the Ethiopian Plateau is thought to be one of the primary mechanisms driving base level fall and incision of the Tekeze River (Pik et al., 2003; Gani, 2015; Blackburn, 2016; Gani and Neupane, 2018; Xue et al., 2018; Bowden, 2018). Other factors include Cenozoic global cooling and Pleistocene glacial cycles that may influence incision. However, due to the proximity to the Equator this area is least affected by these two climatic events (Molnar and England 1990; Gani et al., 2007). The East African climate has also undergone a steady aridification since the Neogene (Cerling et al., 1997; Cane and Molnar, 2001), aiding negligible influence on incision. The second phase of rapid incision ~6 Ma holds the least discernable evidence

from thermal history models. Cooling samples experienced from incision in this phase is attribute to more recent and localized tectonic events as indicated in the nearby Kenyan Rift system in Spiegel et al. (2007) with recent Neogene cooling and/or climate changes due to the sporadic nature of unclear cooling paths that reside close to present day surface temperatures. In summary (Fig. 5.1), the incision history of the Northwestern Ethiopian Plateau is described as episodic where the rapid incision occurred ~12 Ma which is in concert with the increased incision rate of 100m/Ma (Gani, 2015), with another possible phase of young incision coeval with ~6 Ma that supports the third phase of incision described by Gani et al., (2007).

6. CONCLUSION

This study integrates single-grain apatite (U-Th)/He and AFT dates and thermal history modeling of a suite of basement rocks collected from the Tekeze River Canyon to better understand the incision history of the Northwestern Ethiopian Plateau. The youngest thermochronologic cooling ages in the Ethiopian Plateau landscape are provided and implemented to a thermal modeling approach which integrates the replication of measured and predicted data into separate statistically formulated inverse t-T modeling software QTQT and HeFTy. Results indicate that the landscape of the northwestern Ethiopian Plateau evolved significantly after the 30 Ma flood basalt event. Through statistical observation of contributing factors to cooling age spread and radiation damage prevalence, the most significant models of the lowest and youngest elevation sample E-35-17 demonstrates the most significant amounts of recent cooling from the incision of the Tekeze River into the Northwestern Ethiopian Plateau at ~12 and ~6 Ma. The present-day plateau landscape is most likely affected by increased periods of incision required to modify its landform dictated by base level changes attribute to local tectonic influences of the Ethiopian Plateau Uplift in the Northwestern Tekeze River Basin region. The consequential incision history of the Tekeze River into the Northwestern Ethiopian Plateau supported by the thermal models produced in this study is summarized as follows:

 >60-30 Ma: Exhumation and cooling occurred evidenced from modeled rapid cooling gradients from AFT cooling ages, partially reset AHe (E-38-17, E-40-17) cooling ages, and unaffected AHe (E-43-17) cooling ages.

30 Ma: Widespread Ethiopian Flood basalts eruption occurred (Hofmann et al., 1997) locally overburdened samples in the study area up to ~500-1000 m, partially reset (E-40-17 and E-38-17) and near completely resetting (E-35-17) AHe systems.

28 Ma: Initiation of uplift and incision occurs, beginning process of exhuming samples. This early incision is resultant of the elevated topography and incision development continuing to present day.

~12-6 Ma: First phase of rapid cooling and incision occurs, indicated by thermal models of sample E-35-17. This phase agrees with the timing of the transition to rapid incision rates of 100m/Ma in the Tekeze River concluded in Gani (2015), contrasting the conclusion of a majority of incision and uplift occurring between 29-25 Ma from Pik et al. (2003).

6 Ma-Present: A second phase of rapid incision and uplift is perceived to continue to present day, with totality of rates non-discernable due to the sporadic nature of cooling paths to surface temperatures.

In regard to future studies, we hope the gaps in our findings of this study will encourage future researchers to seek answers to questions that have yet to be discovered at the timing of our research. Such improvements to the understanding of the Pre-30 Ma thermal history of Ethiopia can aid greatly and be beneficial in the development of more precise modeling constraints. In context of the Geography and Geology Department at Western Kentucky University, we encourage future students to make use of our left over material separated from collected samples that include entire suites of separated Zircon mineral aggregates.

7. REFERENCES

Abbate, E., Bruni, P., Sagri, M., 2015. Geology of Ethiopia: A Review and Geomorphological Perspectives. Landscapes and Landforms of Ethiopia. World Geomorphological Landscapes 3(389), pp. 33-64. doi: 10.1007/978-94-017-8026-1_2.

Abebe, G., 2017. Long-term climate data description in Ethiopia. Data in Brief, pp. 2352-3409. http://dx.doi.org/10.1016/j.dib.2017.07.052.

Abdelsalam, M.G., Stern, R.J., 1996. Sutures and shear zones in the Arabian-Nubian Shield. Journal of African Earth Sciences 23(3), pp. 289-310.

Adamson, D., Williams, M., 1988. Geological setting of the Pliocene rifting and deposition in the Afar Depression of Ethiopia. Journal of Human Evolution 16, pp. 597-610. doi: https://doi.org/10.1016/0047-2484(87)90015-7.

Beyth, M., Avigad, D., Wetzel, H.U., Matthews, A., Berhe, S.M., 2003. Crustal exhumation and indications for Snowball Earth in the East African Orogen: north Ethiopia and east Eritrea. Precambrian Research 123(2-4), pp.187-201.

Binks, R., Fairhead, J., 1992. A plate tectonic setting for Mesozoic rifts of West and Central Africa. Tectonophysics 213, pp. 141-151. doi: https://doi.org/10.1016/0040-1951(92)90255-5

Blackburn, N. C., 2016. Apatite Helium Thermochronology of the Blue Nile Canyon, Ethiopian Plateau. Masters Theses & Specialist Projects. Western Kentucky University Paper 1563.

Bonini, M., Corti, G., Innocenti, F., Manetti, P., Mazzarini, F., Abebe, T., Pecskay, Z., 2005. Evolution of the Main Ethiopian Rift in the frame of Afar and Kenya rifts propagation. Tectonics 24. doi:10.1029/2004TC001680.

Bowden, S., 2018. Unroofing History of the Northwestern Ethiopian Plateau: Insights from Low-Temperature Apatite Thermochronology. Masters Theses & Specialist Projects. Western Kentucky University Paper 3085.

Bussert, R., Schrank, E., 2007. Palynological evidence for a latest Carboniferous-Early Permian glaciation in Northern Ethiopia. Journal of African Earth Sciences 49(4-5), pp. 201-210.

Cane, M.A., Molnar, P., 2001. Closing of the Indonesian seaway as a precursor to east African aridification around 3–4 million years ago. Nature 411(6834), pp.157.

Cerling, T.E., Harris, J.M., MacFadden, B.J., Leakey, M.G., Quade, J., Eisenmann, V., Ehleringer, J.R., 1997, Global vegetation change through the Miocene/Pliocene boundary: Nature 389, pp. 153–158, doi: 10.1038/38229.

Chorowicz, J., 2005. The East African rift system. Journal of African Earth Sciences 43, 379-410. doi:10.1016/j.jafrearsci.2005.07.019.

Civiero, C., Hammond, J.O., Goes, S., Fishwick, S., Ahmed, A., Ayele, A., Doubre, C., Goitom, B., Keir, D., Kendall, J.M., Leroy, S., 2015. Multiple mantle upwellings in the transition zone beneath the northern East-African Rift system from relative P-wave travel-time tomography. Geochemistry, Geophysics, Geosystems 16(9), pp. 2949-2968.

Clark, M., House, M., Royden, L., Whipple, K., Burchfiel, B., Zhang, X., Tang, W., 2005. Late Cenozoic uplift of southeastern Tibet. Geology 33(6), pp. 525-528. doi:10.1130/G21265.1.

Corti, G., 2009. Continental rift evolution: from rift initiation to incipient break-up in the Main Ethiopian Rift, East Africa. Earth-science reviews 96(1-2), pp.1-53.

Davis, P., Slack, P., 2002. The uppermost mantle beneath the Kenya dome and relation to melting, rifting and uplift in East Africa. Geophysical Research Letters 29(7), 1117. doi: 10.1029/2001GL013676.

Dodson, M.H., 1973. Closure temperature in cooling geochronological and petrological systems. Contributions to Mineralogy and Petrology 40(3), pp. 259-274.

Donelick, R.A., O'Sullivan, P.B., Ketcham, R.A., 2005. Apatite fission-track analysis. Reviews in Mineralogy and Geochemistry 58(1), pp. 49-94.

Ebinger, C., Sleep, N., 1998. Cenozoic magmatism throughout east Africa resulting from impact of a single plume. Nature 395, pp. 788-791. doi:10.1038/27417.

Ebinger, C., Yemane, T., Woldegabriel, G., Aronson, J., Walter, R., 1993. Late Eocene-Recent volcanism and faulting in the southern main Ethiopian Rift. Journal of the Geological Society, London 150, pp. 99-108. doi: https://doi.org/10.1144/gsjgs.150.1.0099.

Ehlers, T.A., Farley, K.A., 2003. Apatite (U–Th)/He thermochronometry: methods and applications to problems in tectonic and surface processes. Earth and Planetary Science Letters 206(1-2), pp.1-14.

Fitzgerald, P.G., Baldwin, S.L., Webb, L.E., O'Sullivan, P.B., 2006. Interpretation of (U–Th)/He single grain ages from slowly cooled crustal terranes: a case study from the Transantarctic Mountains of southern Victoria Land. Chemical Geology 225(1-2), pp. 91-120.

Flowers, R.M., Kelley, S.A., 2011. Interpreting data dispersion and "inverted" dates in apatite (U–Th)/He and fission-track datasets: an example from the US midcontinent. Geochemica et Cosmochemica Acta 75(18), pp. 5169-5186.

Flowers, R.M., Ketcham, R.A., Shuster, D.L., Farley, K.A., 2009. Apatite (U–Th)/He thermochronometry using a radiation damage accumulation and annealing model. Geochemica et Cosmochemica Acta 73(8), pp. 2347-2365.

Flowers, R.M., Wernicke, B., Farley, K., 2008. Unroofing, incision, and uplift history of the southwestern Colorado Plateau from apatite (U-Th)/He thermochronometry. GSA Bulletin 120(5/6), pp. 571-587. doi:10.1130/B26231.1

Fritz, H., Abdelsalam, M., Ali, A., Bingen, B., Collins, S., Fowler, R., Viola, G. 2013. Orogen styles in the East African Orogen: A review of the Neoproterozoic to Cambrian tectonic evolution. Journal of African earth sciences (Oxford, England: 1994) 86, pp. 65–106.

Gallagher, K., 2012. Transdimensional inverse thermal history modeling for quantitative thermochronology. Journal of Geophysical Research: Solid Earth, 117(B2).

Gani, N.D., 2015. Erosion history from incision modeling and river profile morphologies: example from the Tekeze River System, Ethiopian Plateau, East

Africa. Arabian Journal of Geosciences 8(12), pp. 11293-11305. https://doi.org/10.1007/s12517-015-1941-1

Gani, N.D., Neupane, P., 2018. Understanding transient landscape of the Ethiopian Plateau in relation to mantle dynamics. Geological Journal 53, pp. 371-385. doi:10.1002/gj.2903.

Gani, N.D., Abdelsalam, M.G., Gera, S., Gani, M.R., 2009. Stratigraphic and structural evolution of the Blue Nile Basin, Northwestern Ethiopian Plateau. Geological Journal 44, pp. 30-56. doi:10.1002/gj.1127.

Gani, N.D., Gani, M.R., Abdelsalam, M.G., 2007. Blue Nile incision on the Ethiopian Plateau: Pulsed plateau growth, Pliocene uplift, and hominin evolution. GSA Today 17(9), pp. 4-11. doi:10.1130/GSAT01709A.1.

Gavillot, Y., Meigs, A.J., Sousa, F.J., Stockli, D., Yule, D., Malik, M., 2018. Late Cenozoic Foreland-to-Hinterland Low-Temperature Exhumation History of the Kashmir Himalaya. Tectonics 37(9), pp. 3041-3068.

George, R., Rogers, N., 2002. Plume dynamics beneath the African plate inferred from the geochemistry of the Tertiary basalts of southern Ethiopia. Contributions to Mineral and Petrology 144, 286. doi:10.1007/s00410-002-0396-z.

Gleadow, A., Brown, R., 2000. Fission-track thermochronology and the long-term denudation response to tectonics. Geomorphology and Global Tectonics, pp. 57-75.

Hofmann, C., Courtillot, V., Feraud, G., Rochette, P., Yirgu, G., Ketefo, E., Pik, R., 1997. Timing of the Ethiopian flood basalt event and implications of Plume birth and global change. Nature 389, 838-841. doi:10.1038/39853,

Howard, A.D., Dietrich, W.E., Seidl, M.A., 1994. Modeling fluvial erosion on regional to continental scales. Journal of Geophysical Research: Solid Earth 99(B7), pp. 13971-13986.

Humphrey, N., Konrad, S., 2000. River incision or diversion in response to bedrock uplift. Geology 28(1), pp. 43-46. doi:https://doi.org/10.1130/0091-7613(2000)28<43:RIODIR>2.0.CO;2.

Hunegnaw, A., Sage, L., Gonnard, R., 1998. Hydrocarbon potential of the intracratonic Ogaden Basin, SE Ethiopia. Journal of Petroleum Geology 21(4), pp. 401-425.

Ketcham, R.A., 2005. Forward and inverse modeling of low-temperature thermochronometry data. Reviews in mineralogy and geochemistry 58(1), pp. 275-314.

Mangesha, T., Chernet, T., Haro, W., 1996. Geological map of Ethiopia (1:2,000,000), Geological Survey of Ethiopia, Addis Ababa, Ethiopia.

Marty, B., Gezahegn, Y., 1996. Helium isotopic variations in Ethiopian plume lavas: nature of magmatic sources and limit on lower mantle contribution. Earth and Planetary Science Letters 144(1-2), pp. 223-237.

Mock, C., Arnaud, N.O., Cantagrel, J.M., Yirgu, G., 1999. ^{40}Ar/^{39}Ar thermochronology of the Ethiopian and Yemeni basements: reheating related to the Afar plume? Tectonophysics 314(4), pp. 351-372.

Mohr, P., 1983. The Ethiopian flood basalt province. Nature 303, 577-584. doi:10.1038/303577a0.

Molnar P., England P., 1990. Late Cenozoic uplift of mountain ranges and global climate change: chicken or egg? Nature 346, pp. 29–34.

Nie, J., Ruetenik, G., Gallagher, K., Hoke, G., Garzione, C.N., Wang, W., Stockli, D., Hu, X., Wang, Z., Wang, Y., Stevens, T., 2018. Rapid incision of the Mekong River in the middle Miocene linked to monsoonal precipitation. Nature Geoscience 11(12), p. 944.

Pik, R., Marty, B., Carignan, J., Lave, J., 2003. Stability of the Upper Nile drainage network (Ethiopia) deduced from (U-Th)/He thermochronometry: implications for uplift and erosion of the Afar plume dome. Earth and Planetary Science Letters 215, pp. 73-88. doi:10.1016/S0012-821X(03)00457-6.

Pik, R., Marty, B., Carignan, J., Yirgu, G., Teklewold, A., 2008. Timing of East African Rift development in southern Ethiopia: Implication for mantle plume activity and evolution of topography. Geology 36(2), 167-170. doi:10.1130/G24233A.1,

Reiners, P.W., 2002. (U-Th)/He chronometry experiences a renaissance. Eos, Transactions American Geophysical Union 83(3), pp. 21-27.

Reiners, P., Brandon, M., 2006. Using thermochronology to understand orogenic erosion. Annual Review of Earth and Planetary Science 34, pp. 419-466. doi:10.1146/annurev.earth.34.031405.125202.

Reiners, P., Ehlers, T., Zeitler, P., 2005. Past, present, and future of thermochronology. Reviews in Mineralogy and Geochemistry 58, pp. 1-18. doi:10.2138/rmg.2005.58.1.

Reiners, P.W., Farley, K.A., 2001. Influence of crystal size on apatite (U–Th)/He thermochronology: an example from the Bighorn Mountains, Wyoming. Earth and Planetary Science Letters 188(3-4), pp. 413-420.

Ring, U., 2014. The East African rift system. Austrian Journal of Earth Sciences 107(1), 132-146.

Rohrmann, A., Kapp, P., Carrapa, B., Reiners, P., Guynn, J., Ding, L., Heizler, M., 2012. Thermochronologic evidence for plateau formation in central Tibet by 45 Ma. Geology 40(2), 187-190. doi:10.1130/G32530.1.

Schildgen, T., Hodges, K., Whipple, K., Reiners, P., Pringle, M., 2007. Uplift of the western margin of the Andean plateau revealed from canyon incision history, southern Peru. Geology 35(6), 523-526. Doi:10.1130/G23532A.1

Shuster, D., Farley, K., 2005. ^{4}He/^{3}He thermochronometry: theory, practice, and potential complications. Reviews in Mineralogy and Geochemistry 58, pp. 181-203. doi:10.2138/rmg.2005.58.7.

Shuster, D., Farley, K., 2003. ^{4}He/^{3}He thermochronometry. Earth and Planetary Science Letters 217, pp. 1-17. doi:10.1016/S0012-821X(03)00595-8.

Spiegel, C., Kohn, B., Belton, D., Gleadow, A., 2007. Morphotectonic evolution of the central Kenya rift flanks: Implications for late Cenozoic environmental change in East Africa. Geology 35(5), pp. 427-430. doi:10.1130/G23108A.

Spiegel, C., Kohn, B., Belton, D., Berner, Z., Gleadow, A., 2009. Apatite (U–Th–Sm)/He thermochronology of rapidly cooled samples: the effect of He implantation. Earth and Planetary Science Letters 285(1-2), pp.105-114.

Stern, R. J., 1994. Arc Assembly and Continental Collision in the Neoproterozoic East African Orogen: Implications for the Consolidation of Gondwanaland. Annual Reviews, Earth Planet 22, pp. 319-351.

Vermeesch, P., Seward, D., Latkoczy, C., Wipf, M., Günther, D., Baur, H., 2007. α-Emitting mineral inclusions in apatite, their effect on (U–Th)/He ages, and how to reduce it. Geochemica et Cosmochemica Acta 71(7), pp. 1737-1746.

Vermeesch, P., Tian, Y., 2014. Thermal history modelling: HeFTy vs. QTQt. Earth-Science Reviews 139, pp. 279-290.

Versfelt, J., Rosendahl, B.R., 1989. Relationships between pre-rift structure and rift architecture in Lakes Tanganyika and Malawi, East Africa. Nature 337(6205), p. 354.

Wakabayashi, J., Sawyer, T., 2001. Stream incision, tectonics, uplift, and evolution of topography of the Sierra Nevada, California. The Journal of Geology,109, pp. 539-562.

Woldegrabriel, G., Aronson, J., Walter, R., 1990. Geology, geochronology, and rift basin development in the central sector of the Main Ethiopian Rift. Geologic Society of America Bulletin 102, pp. 439-458. doi:10.1130/0016-7606(1990)102<0439:GGARBD>2.3.CO;2.

Wolfenden, E., Ebinger, C., Yirgu, G., Deino, A., Ayalew, D., 2004. Evolution of the northern Main Ethiopian rift: birth of a triple junction. Earth and Planetary Science Letters 224, pp. 213-228. doi:10.1016/j.epsl.2004.04.022

Xue, L., Alemu, T., Gani, N.D., Abdelsalam, M.G., 2018. Spatial and temporal variation of tectonic uplift in the southeastern Ethiopian Plateau from morphotectonic analysis. Geomorphology 309, pp. 98-111.

Yemane, K., Bonnefille, R., Faure, H., 1985. Paleoclimatic and tectonic implications of Neogene microflora from the Northwestern Ethiopian highlands. Nature 318(6047), pp. 653-656.